High-spin spectroscopy and quasiparticle alignments in ^{124,125}Ce

J. F. Smith,[1,*] V. Medina-Chico,[1,†] C. J. Chiara,[2,3] M. P. Carpenter,[4] C. N. Davids,[4] M. Devlin,[3,5] J. L. Durell,[1] D. B. Fossan,[2] S. J. Freeman,[1] R. V. F. Janssens,[4] D. R. LaFosse,[2] M. J. Leddy,[1,‡] P. Reiter,[4] D. G. Sarantites,[3] D. Seweryniak,[4] K. Starosta,[2] R. Wadsworth,[6] A. N. Wilson,[6,§] and J. N. Wilson[3,‖]

[1]*Schuster Laboratory, University of Manchester, Manchester M13 9PL, United Kingdom*

[2]*Department of Physics and Astronomy, State University of New York at Stony Brook, Stony Brook, New York 11794-3800, USA*

[3]*Department of Chemistry, Washington University, St. Louis, Missouri 63130, USA*

[4]*Argonne National Laboratory, Argonne, Illinois 60439, USA*

[5]*LANSCE-3, Los Alamos National Laboratory, Los Alamos, New Mexico 87545, USA*

[6]*Department of Physics, University of York, Heslington, York YO10 5DD, United Kingdom*

(Received 26 July 2003; published 31 March 2004)

Rotational bands have been studied to high spins in the neutron-deficient ^{124,125}Ce nuclei. The nuclei were populated using the ^{64}Zn(^{64}Zn,$2p2n$)^{124}Ce and ^{64}Zn(^{64}Zn,$2pn$)^{125}Ce reactions, with a beam energy of 260 MeV. High-fold γ-ray coincidence data were collected using the Gammasphere germanium-detector array. The Microball charged-particle detector array was used to provide channel selection. The previously established level structures of both ^{124,125}Ce have been extended to high spins ($\sim 30\hbar$). In addition, several new bands have been identified. The alignments of pairs of $h_{11/2}$ neutrons and protons are observed in both nuclei. The alignments are compared to the predictions of Woods-Saxon cranked shell model calculations and to the systematics of $h_{11/2}$ quasiparticle alignments in neighboring nuclei. The apparent ability of the cranked shell model to explain the $h_{11/2}$ neutron alignments in ^{124,125}Ce highlights the previously reported discrepancies between experiment and theory for the ^{128}Ce isotope and, to a lesser extent, ^{126}Ce.

DOI: 10.1103/PhysRevC.69.034339 PACS number(s): 21.10.Re, 23.20.Lv, 27.60.+j, 29.30.Kv

I. INTRODUCTION

The neutron-deficient $Z=58$ cerium isotopes with $A<130$ are well deformed, with quadrupole deformations of $\beta_2 = 0.25-0.30$ [1]. Consequently, γ-ray spectroscopy of these nuclei is dominated by rotational bands, built on the ground and low-lying excited states. The behavior of these rotational bands can provide useful information about the underlying nuclear structure. For example, rotational alignments of pairs of both neutrons and protons from the $h_{11/2}$ subshells are predicted at reasonably low rotational frequencies ($\leqslant 0.5$ MeV$/\hbar$) in these isotopes. The exact details of the alignments are often sensitive to the underlying quasiparticle configurations or to the deformations. In the isotopes ^{126,128}Ce [2,3] discrepancies have been reported between the predicted and observed behavior at the first $h_{11/2}$ neutron alignments in the yrast bands, and it is unclear whether similar discrepancies persist in the lighter isotopes. In addition to extracting information from alignment properties, the ground-state deformation can be estimated from the excitation energy of the first 2^+ state [4–6]. Using this method, it has been shown [7] that the ground-state deformations of the even-even cerium isotopes increase as the neutron number N moves away from the closed shell at $N=82$, towards midshell at $N=66$. However, for the lightest cerium isotope in which excited states have been identified, ^{124}Ce, the energy of the 2^+ state suggests that the ground-state deformation is larger than predicted by calculations [8]. The reason for this enhanced deformation is still not understood, and insight into this phenomenon could be gained if the structure of nuclei near ^{124}Ce were better understood.

In order to investigate these issues, an experiment has been performed to study ^{124,125}Ce at high spin. Several new band structures have been identified and studied in both nuclei. The ^{64}Zn(^{64}Zn) reaction has been used in an experiment with Gammasphere [9] and the Microball [10]. Previous experimental studies of these isotopes are briefly summarized in Sec. I, experimental details and data analysis methods are given in Secs. II and III, and the results are presented and discussed in Secs. IV and V.

The nuclei ^{124,125}Ce have been studied in several previous experiments. Three γ-ray transitions were first assigned to both ^{124,125}Ce in an experiment by James *et al.* [11] using the Daresbury recoil-mass separator [12]. Following that work, Ying *et al.* [8] first studied the yrast band of ^{124}Ce up to spin $14\hbar$, and later [13] extended the yrast band to $24\hbar$. In the later work [13] ^{125}Ce was populated and two strongly coupled rotational bands were identified. Osa *et al.* [14] identified three γ-ray transitions in ^{125}Ce following the β^+/EC decay of ^{125}Pr. Recently, ^{125}Ce has been studied by Paul *et al.* [15]. Their work confirmed the work of Ying *et al.*; the same two bands were observed, and were extended to spins $27/2\hbar$ and $17/2\hbar$. In the period since the present work was completed, a separate study of ^{125}Ce has been made in Ref.

*Electronic address: john.f.smith@man.ac.uk

†Present address: Universidad Autónoma de Madrid, Spain.

‡Present address: NNC Ltd., Chelford Road, Knutsford, Cheshire WA16 8QZ, UK.

§Present address: Australian National University, Canberra ACT 0200, Australia.

‖Present address: The Niels Bohr Institute, University of Copenhagen, 4000 Roskilde, Denmark.

TABLE I. Lists of gating transitions used to project the spectra shown in Figs. 1–4. Any one of these gates must be satisfied when the list is used. In the right-hand column, for example, "142 keV−559 keV" means all transitions (inclusive) between the 142 and 559 keV transitions in that band, ordered by the spin of the initial states. The lists which were used for each spectrum are indicated in the captions of Figs. 1–4.

List	Transition energies
a	142 keV to 559 keV in ^{124}Ce Band 1
b	650 keV to 1129 keV in ^{124}Ce Band 1
c	142 keV to 444 keV in ^{124}Ce Band 1
d	142 keV to 650 keV in ^{124}Ce Band 1
e	142 keV to 851 keV in ^{124}Ce Band 1
f	851 keV to 1230 keV in ^{124}Ce Band 1
g	808 keV to 1043 keV in ^{124}Ce Band 2
h	590 keV to 980 keV in ^{124}Ce Band 3
i	135 keV and 167 keV in ^{125}Ce Band 1
j	660 keV to 1227 keV in ^{125}Ce Band 1
k	707 keV to 1397 keV in ^{125}Ce Band 1
l	147 keV and 181 keV in ^{125}Ce Band 2
m	600 keV to 888 keV in ^{125}Ce Band 2
n	976 keV to 1167 keV in ^{125}Ce Band 2
o	635 keV to 1255 keV in ^{125}Ce Band 2
p	743 keV to 1328 keV in ^{125}Ce Band 3
q	551 keV to 1214 keV in ^{125}Ce Band 3

[16] by Petrache *et al.* The results of the work by Paul *et al.* and Petrache *et al.* are discussed in Sec. IV. The ground state of ^{125}Ce has been assigned to have spin $5/2$ by Wilmarth *et al.* [17], by comparing the intensities of transitions in ^{124}Ba to statistical model calculations, following the β-delayed proton decay of ^{125}Ce.

II. EXPERIMENTAL DETAILS

The work described here has been presented in detail in Ref. [18]. In this work, excited states in ^{124,125}Ce have been populated using the ^{64}Zn(^{64}Zn,$2p2n$) and ^{64}Zn(^{64}Zn,$2pn$) reactions, respectively. The 260-MeV ^{64}Zn beam was provided by the Argonne Tandem-Linac Accelerator System (ATLAS) at Argonne National Laboratory. The beam was incident upon a target, made of a 750-μg/cm^2 self-supporting foil. At the time of this experiment, Gammasphere had 101, 75%-efficient Compton-suppressed germanium detectors in place. The detectors were arranged in rings of constant polar angle θ; three detectors at $\theta=31.7°$, five at 37.4°, ten at 50.1°, five at 58.3°, ten at 69.8°, five at 79.2°, five at 80.7°, eight at 90.0°, five at 99.3°, five at 100.8°, ten at 110.2°, five at 121.7°, ten at 129.9°, five at 142.6°, five at 148.3°, and five at 162.7°. The Microball charged-particle detector array was used in conjunction with Gammasphere. The Microball is described comprehensively in Ref. [10]. In essence, it consists of 95 CsI(Tl) scintillators, arranged in nine rings of constant θ, covering $\approx$97% of 4π. The Microball is used to detect evaporated protons and α particles with high efficiency, in coincidence with γ rays in Gammasphere. In addition, the Argonne Fragment Mass Analyser (FMA) [19] was used in order to determine the mass of evaporation residues. However, in this particular experiment, a problem with the trigger map prevented a substantial fraction of the high γ-ray fold events which included FMA data from being recorded, effectively destroying the efficacy of the FMA for the purpose of this particular analysis. With the condition that four unsuppressed germanium detectors had to fire before data were recorded, $\approx 820\times10^6$ events were collected during the 2.5-day experiment.

III. ANALYSIS METHODS

A. α-particle and proton detection

The Microball was used to determine the evaporated α-particle and proton multiplicity in coincidence with an event in Gammasphere. In order to discriminate between α particles and protons, three parameters associated with each Microball pulse were written into the data. Specifically these parameters were (i) the energy, integrated over the first 1 μs

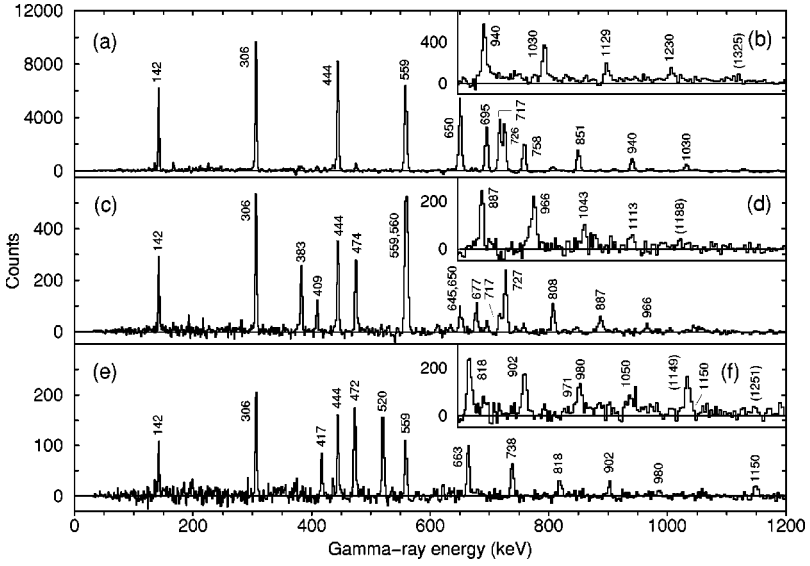

FIG. 1. Spectra showing bands in ^{124}Ce, projected from the particle-gated cube. Panels (a) and (b) show Band 1, (c) and (d) show Band 2, and (e) and (f) show Band 3. The spectra are double gated, using lists of gates given in Table I: (a) is gated by lists a and b (or [a/b]); (b) is gated on [e/f]; (c) is gated on [c/645]; (d) is gated on [d/g]; (e) is gated on [c/590]; and (f) is gated on [d/h]. The peaks are marked with the γ-ray transition energies given to the nearest keV. The energies in parentheses correspond to transitions which are tentatively placed in coincidence.

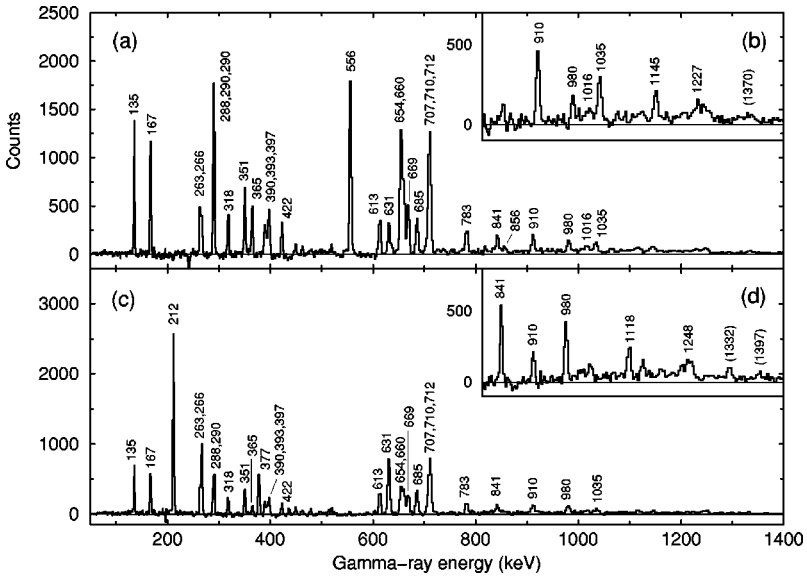

FIG. 2. Spectra showing transitions in ^{125}Ce Band 1, projected from the particle-gated cube. The spectra are double-gated using lists of gates given in Table I: (a) is gated on [i/436]; (b) is gated on [i/j]; (c) is gated on [i/515]; and (d) is gated on [i/k]. The 1016-keV peak in panel (b) presumably arises from overlap of the 654-keV peak and the 660-keV peak in list i. The peaks are marked with the γ-ray transition energies given to the nearest keV. The energies in parentheses correspond to transitions which are tentatively placed in coincidence.

of the pulse; (ii) the PID (an abbreviation of "particle identification") which is an energy integrated over 10 ns, 9 μs after the start of the pulse; and (iii) the time between the rf signal of ATLAS and the pulse. By plotting various combinations of these three parameters, excellent separation of protons and α particles was achieved [10]. Consequently, detection efficiencies were found to be 82% for protons and 60% for α particles.

B. γ-ray spectra

The data were sorted off-line into 3d-histograms or "cubes," with γ-ray energy on each of the three axes. The mean unsuppressed γ-ray fold was found to be 4.3. Each n-fold event was unfolded into $^nC_3$ threefold events, which were used to increment the cubes. For this analysis, two cubes were created. The first *ungated* cube was incremented with all of the events in the data set, and contained 7.5 $\times 10^9$ counts. The second cube was incremented only with events in coincidence with either exactly one proton or exactly two protons in the Microball and this cube contained 2.2×10^9 counts. This *particle-gated* cube was constructed in order to enhance the relative content of the $2pn$(^{125}Ce) and $2p2n$(^{124}Ce) evaporation channels. The RADWARE [20] code LEVIT8R was used to project one-dimensional background-subtracted double-gated spectra from the cubes. By projecting spectra from the ungated cube, $\approx$15 nuclei were identified in the data. The most intensely populated nuclei were ^{122}Ba and ^{125}La which were populated with fractions of 35% and 15% of the total data set, respectively. The nuclei ^{124}Ce and ^{125}Ce were populated with fractions of $\approx$5% and 10% of the data, respectively, which (assuming a total evaporation-residue cross section of 500 mb, calculated using the code ALICE [21]) correspond to cross sections of 20 and 40 mb. Representative spectra from the particle-gated cube are shown in Fig. 1 for ^{124}Ce, and Figs. 2–5 for ^{125}Ce.

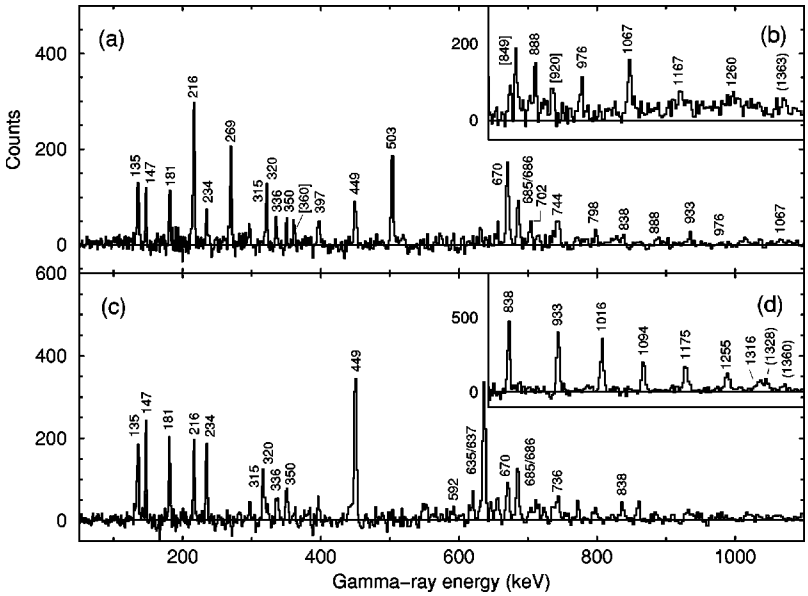

FIG. 3. Spectra showing transitions in ^{125}Ce Band 2, projected from the particle-gated cube. The spectra are double gated using lists of gates given in Table I: (a) is gated on [1/600]; (b) is gated on [m/n]; (c) is gated on [1/554]; and (d) is gated on [o/o], excluding self-coincidences. The peaks are marked with the γ-ray transition energies given to the nearest keV. The energies in parentheses correspond to transitions which are tentatively placed in coincidence; those in square brackets could not be placed in the level scheme.

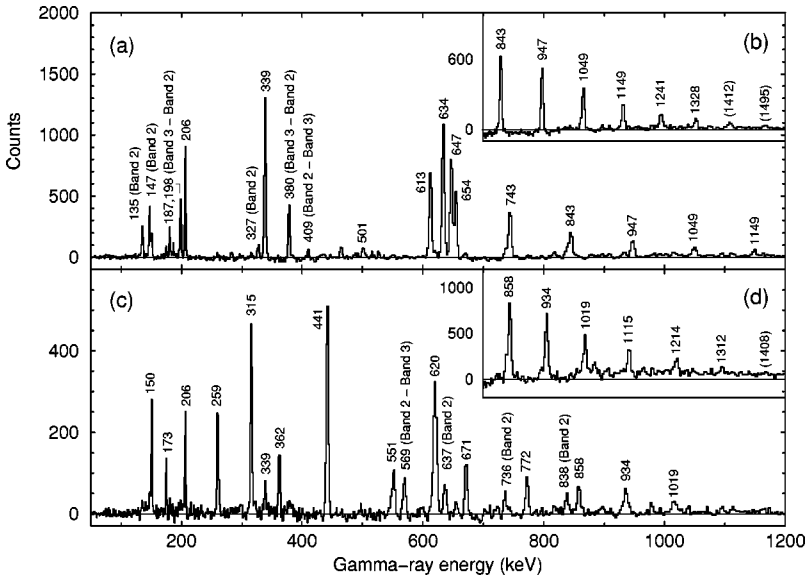

FIG. 4. Spectra showing transitions in ^{125}Ce Band 3, projected from the particle-gated cube. The spectra are double-gated using lists of gates given in Table I: (a) is gated on [465/562]; (b) is gated on [465/p]; (c) is gated on [547/620]; and (d) is gated on [q/q], excluding self-coincidences. The peaks are marked with the γ-ray transition energies given to the nearest keV. The energies in parentheses correspond to transitions which are tentatively placed in coincidence.

C. Angular-intensity measurements

In order to help assign relative spins and parities to the excited states, a type of γ-ray angular-distribution measurement was performed. Two γ-γ matrices were constructed, which were incremented with γ-ray energies from any germanium detector on one axis, and with γ-ray energies from detectors at a particular value of θ on the other axis. [In order to increase the number of counts, detectors at θ and $(180° - \theta)$ were summed.] These matrices were also only incremented when exactly one or exactly two protons were detected by the Microball, thus enhancing the relative amount of ^{124}Ce and ^{125}Ce in the data. By gating on the "any" germanium-detector axis, the intensities of γ rays at a particular θ could be measured. Using this method, γ-ray intensities at $\theta \simeq 90°$ (28 detectors at $\theta = 79.2°$, 80.7°, 90.0°, 99.3°, and 100.8°) and $\theta \simeq 40°$ (38 detectors at $\theta = 31.7°$, 37.4°, 50.1°, 129.9°, 142.6°, and 148.3°) were measured, and the angular-intensity ratio R_θ of these intensities was taken. After normalization, R_θ was found to be near 0.7 for a stretched-dipole transition and near 1.3 for a stretched-quadrupole transition. These values were calibrated using known transitions in the well-studied ^{126}Ce [2,22] and ^{124}Ba [23] nuclei.

IV. RESULTS

A. Level schemes

Coincidence relationships, together with energy- and intensity-balance arguments, have been used to deduce the level schemes presented in Fig. 6 for ^{124}Ce and Fig. 7 for ^{125}Ce. Three bands have been observed in ^{124}Ce and four bands in ^{125}Ce. The spins and parities given in the figures have been assigned using angular-intensity measurements described in the preceding section, together with the systematics of neighboring nuclei. The relative spin assignments were made up to the following spins: ^{124}Ce Band 1, $20\hbar$; ^{124}Ce Band 2, $19\hbar$; ^{124}Ce Band 3, $20\hbar$; ^{125}Ce Band 1, $45/2\hbar$; ^{125}Ce Band 2, $27/2\hbar$; ^{125}Ce Band 3, $53/2\hbar$; and two transitions in ^{125}Ce Band 4 were shown to have stretched-quadrupole character, but the spin relative to the other bands

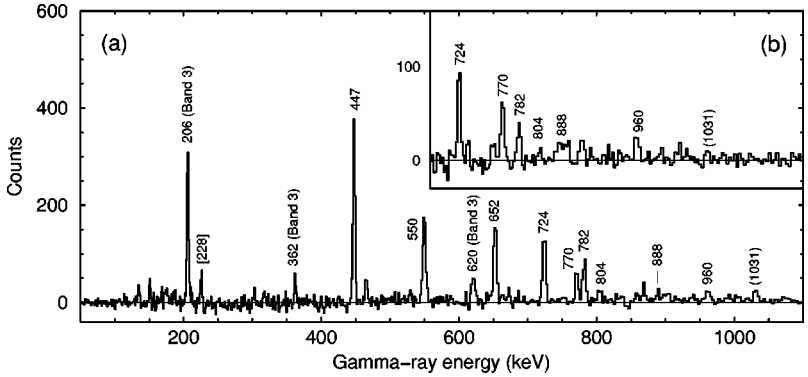

FIG. 5. Spectra showing transitions in ^{125}Ce Band 4, projected from the particle-gated cube. Spectrum (a) is gated on [338/549] and (b) is a sum of two spectra gated on [447/770] and [550/652]. The 206-, 362-, and 620-keV transitions in panel (a) presumably arise from the [339/547] contribution (where both transitions are in Band 3) to the [338/549] gate. The peaks are marked with the γ-ray transition energies given to the nearest keV. The energies in parentheses correspond to transitions which are tentatively placed in coincidence. The 228-keV transition, with energy in square brackets, appeared to be in coincidence but could not be placed in the level scheme.

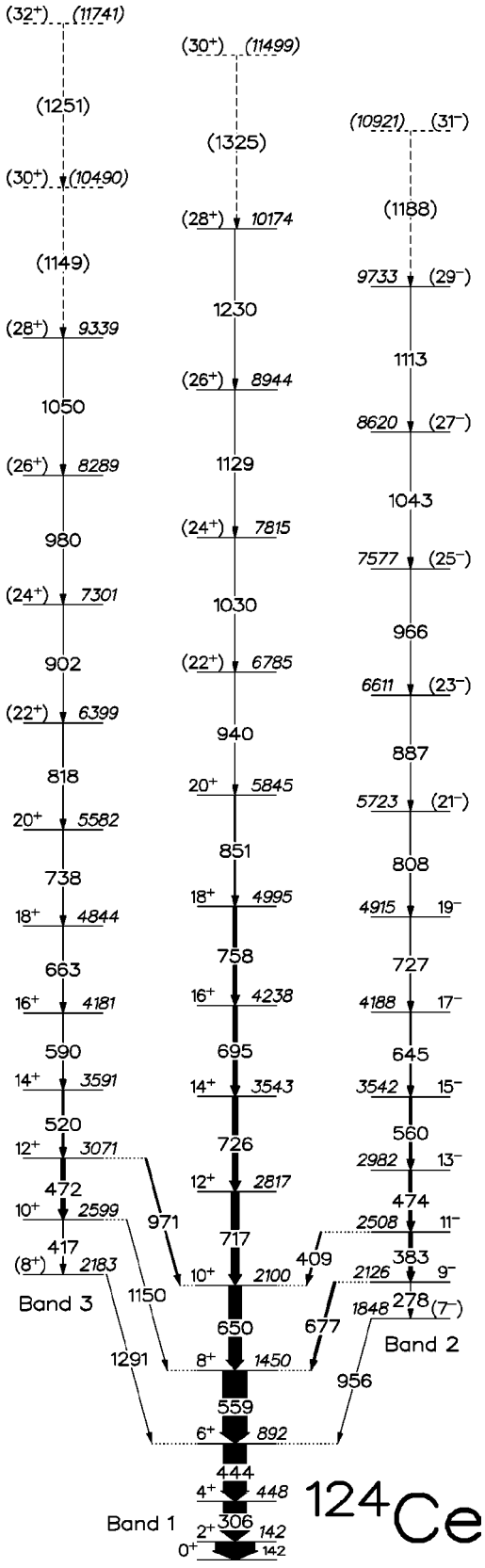

FIG. 6. The level scheme of ^{124}Ce deduced in this work. The measured properties of the transitions are given in Table II. Spins and parities in parentheses are tentatively assigned, and dashed transitions, with energies in parentheses, are tentatively placed.

has not been established. All of the measured properties of the γ-ray transitions in ^{124}Ce and ^{125}Ce, observed in this work, are given in Tables II and III, respectively. The level energies are given in the figures; where there is more than one path to the ground state, the level energies have been fitted using the RADWARE code LEVIT8R.

1. ^{124}Ce

Three rotational bands have been observed in ^{124}Ce. Representative coincidence spectra showing the transitions in the three bands are presented in Fig. 1. The ground-state band has been labeled Band 1, and two additional bands have been observed, labeled Bands 2 and 3, which feed into Band 1 over the spin range $6\hbar-10\hbar$. All three bands consist of decoupled sequences of $\Delta I=2$ $E2$ transitions. Three transitions decay from Band 2 into Band 1 (956 keV, 677 keV, and 409 keV). The measured R_θ values of the 409- and 677-keV transitions (Table II) suggest that they have stretched-dipole character, consistent with a negative-parity assignment for Band 2. (If the band were of positive parity, mixed $M1/E2$ transitions may be observed.) It should be pointed out here that an analogous band is observed in the neighboring even-even isotone ^{122}Ba: recent polarization and angular-distribution measurements have shown the linking transitions in that case to have $E1$ multipolarity, giving the analogous band negative parity [24]. Similarly, three transitions decay from Band 3 into Band 1 (1291 keV, 1151 keV, and 971 keV). The measured R_θ values of these transitions are consistent with stretched-quadrupole multipolarity. Weisskopf estimates suggest that the transitions are more likely to have $E2$ rather than $M2$ character, suggesting that Band 3 has positive parity. Given the spin assignments in Fig. 6, Band 1 extends to spin $28\hbar$ (tentatively $30\hbar$), Band 2 to $29\hbar$ (tentatively $31\hbar$), and Band 3 to $28\hbar$ (tentatively $32\hbar$).

2. ^{125}Ce

The level scheme of ^{125}Ce is shown in Fig. 7. Four rotational bands have been observed, labeled Bands 1 to 4. The most intensely populated band is Band 1 (which takes about 40% of the intensity of the ^{125}Ce channel) followed by Band 3 (30%), Band 2 (25%), and Band 4 (5 %). Bands 1 and 2 were previously observed by Ying *et al.* [13] and Paul *et al.* [15].

Both $\Delta I=2$ signature partners of Band 1 are observed to high spin. The $\alpha=-1/2$ sequence is observed to $55/2\hbar$ (tentatively $59/2\hbar$) and the $\alpha=+1/2$ sequence is observed to $53/2\hbar$ (tentatively $61/2\hbar$). The signature splitting is very small over the observed frequency range ($\sim$0 at 0.5 MeV/$\hbar$). Within the band, $\Delta I=1$ $M1/E2$ transitions are observed to connect the two signature partners below spin $45/2\hbar$. In addition, two transitions, with energies 1016 keV and 856 keV, are observed to feed into the $27/2^-$ state; these transitions have low intensity and, without extension of the structure to higher spins, it is not possible to attempt a more detailed analysis or a discussion of their origin.

Band 2 also consists of two $\Delta I=2$ signature partners. In this band, the $\alpha=-1/2$ sequence is observed to $67/2\hbar$ (tentatively $75/2\hbar$) and the $\alpha=+1/2$ sequence is observed to

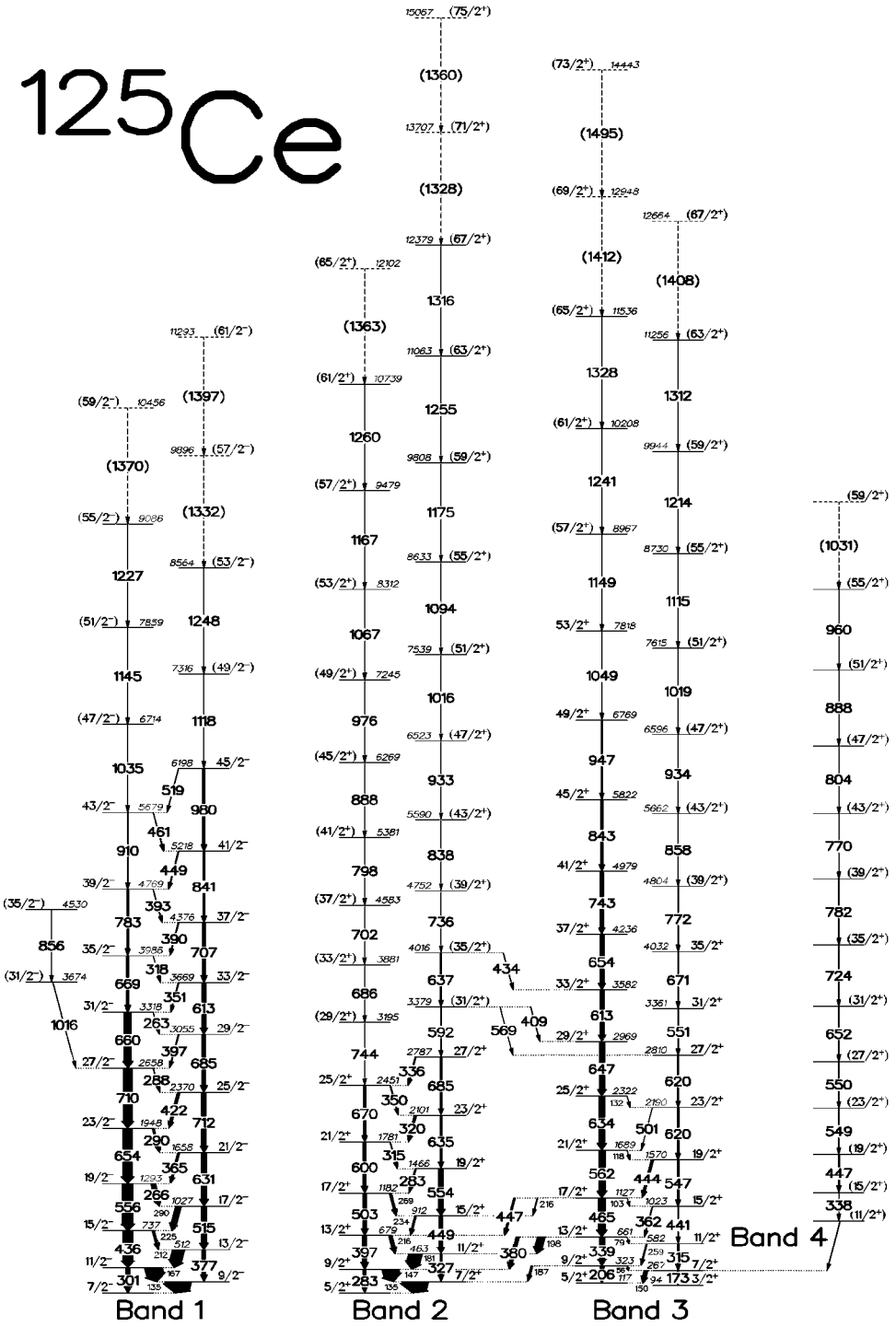

FIG. 7. The level scheme of ^{125}Ce deduced in this work. The measured properties of the transitions are given in Table III. Spins and parities in parentheses are tentatively assigned, and dashed transitions, with energies in parentheses, are tentatively placed. The spins of Band 4 are estimated.

$61/2\hbar$ (tentatively $65/2\hbar$). Below a rotational frequency of about 0.35 MeV/$\hbar$, the signature splitting is essentially zero. Below spin 27/2, $\Delta I=1$ $M1/E2$ interband transitions are observed to connect the two signature partners.

In Band 3, like Bands 1 and 2, both signature partners are observed to high spin. In this band, the $\alpha=-1/2$ sequence is observed to $63/2\hbar$ (tentatively $67/2\hbar$) and the $\alpha=+1/2$ sequence is observed to $65/2\hbar$ (tentatively $73/2\hbar$). This band has larger signature splitting than either Band 1 or 2; at 0.5 MeV/$\hbar$, the signature splitting is 280 keV. Below spin 25/2, $\Delta I=1$ $M1/E2$ transitions are observed to link the two signature partners.

As can be seen in Fig. 7, eight transitions have been observed connecting Bands 2 and 3. At low spin, five transitions decay from Band 3 into Band 2. Three of these transitions, with energies 187, 198, and 216 keV, have R_θ values consistent with stretched-dipole character, and are presumed to be $M1/E2$ transitions. Two transitions observed decaying from Band 3 to Band 2, with energies 380 and 447 keV, have R_θ values consistent with stretched-quadrupole character, and are presumed to be $E2$ transitions. At higher spins, three transitions with energies 409, 434, and 569 keV decay from Band 2 into Band 3. The R_θ value of the 569-keV transition suggests that it has $E2$ character. Although the low intensities

TABLE II. Properties of γ-ray transitions in ^{124}Ce. The intensities, given in the second column from the left, are normalized to the intensity of the 141.9-keV($2^+ \rightarrow 0^+$) transition having an arbitrary 100 units. The given multipolarities are inferred from the angular-intensity ratios R_θ and from systematics. The spins and multipolarities in parentheses are tentative. The transitions with energies marked by a superscript letter *t* are placed tentatively in the level scheme.

E_γ (keV)	I_γ (%)	$I_i^\pi \rightarrow I_f^\pi$	R_θ	Multipolarity
141.9 (2)	100 (2)	$2^+ \rightarrow 0^+$	1.15 (2)	$E2$
277.8 (2)	1.9 (6)	$9^- \rightarrow (7^-)$		$(E2)$
305.9 (2)	59 (1)	$4^+ \rightarrow 2^+$	1.24 (2)	$E2$
382.5 (2)	7.7 (3)	$11^- \rightarrow 9^-$	1.52 (6)	$E2$
408.7 (2)	3.2 (2)	$11^- \rightarrow 10^+$	0.75 (4)	$E1$
416.6 (2)	4 (1)	$10^+ \rightarrow (8^+)$		$(E2)$
444.1 (2)	57 (1)	$6^+ \rightarrow 4^+$	1.28 (3)	$E2$
472.3 (2)	4 (1)	$12^+ \rightarrow 10^+$	1.6 (1)	$E2$
474.2 (2)	8.7 (6)	$13^- \rightarrow 11^-$	1.41 (2)	$E2$
520.3 (2)	5.8 (4)	$14^+ \rightarrow 12^+$		$(E2)$
558.9 (2)	50 (5)	$8^+ \rightarrow 6^+$	1.56 (4)	$E2$
559.9 (2)	6 (1)	$15^- \rightarrow 13^-$	1.46 (3)	$E2$
590.1 (2)	3.3 (8)	$16^+ \rightarrow 14^+$	1.6 (2)	$E2$
645.3 (2)	3.3 (6)	$17^- \rightarrow 15^-$	1.32 (6)	$E2$
649.6 (2)	33 (1)	$10^+ \rightarrow 8^+$	1.47 (7)	$E2$
663.3 (2)	2.7 (7)	$18^+ \rightarrow 16^+$	1.6 (1)	$E2$
677.4 (2)	5.8 (3)	$9^- \rightarrow 8^+$	0.82 (3)	$E1$
694.6 (2)	11 (1)	$16^+ \rightarrow 14^+$	1.26 (4)	$E2$
717.4 (2)	21 (1)	$12^+ \rightarrow 10^+$	1.34 (8)	$E2$
726.3 (2)	15 (1)	$14^+ \rightarrow 12^+$	1.39 (8)	$E2$
727.4 (2)	2.0 (4)	$19^- \rightarrow 17^-$	1.32 (5)	$E2$
738.3 (2)	1.6 (4)	$20^+ \rightarrow 18^+$	1.6 (1)	$E2$
758.3 (2)	8 (1)	$18^+ \rightarrow 16^+$	1.41 (6)	$E2$
807.5 (2)	1.3 (2)	$(21^-) \rightarrow 19^-$		$(E2)$
818.2 (2)	1.3 (4)	$(22^+) \rightarrow 20^+$		$(E2)$
850.6 (2)	3.7 (2)	$20^+ \rightarrow 18^+$	1.34 (7)	$E2$
887.0 (2)	0.5 (1)	$(23^-) \rightarrow (21^-)$		$(E2)$
902 (1)		$(24^+) \rightarrow (22^+)$		$(E2)$
940.0 (2)	2.2 (1)	$(22^+) \rightarrow 20^+$		$(E2)$
956 (1)		$(7^-) \rightarrow 6^+$		$(E1)$
966.4 (2)	0.26 (9)	$(25^-) \rightarrow (23^-)$		$(E2)$
971.2 (2)	3.5 (3)	$12^+ \rightarrow 10^+$	1.36 (8)	$E2$
980 (1)	0.8 (2)	$(26^+) \rightarrow (24^+)$		$(E2)$
1030 (1)	1.5 (4)	$(24^+) \rightarrow (22^+)$		$(E2)$
1043 (1)	0.15 (5)	$(27^-) \rightarrow (25^-)$		$(E2)$
1050 (1)	0.7 (2)	$(28^+) \rightarrow (26^+)$		$(E2)$
1113 (1)	0.10 (5)	$(29^-) \rightarrow (27^-)$		$(E2)$
1129 (1)	0.6 (2)	$(26^+) \rightarrow (24^+)$		$(E2)$
1149^t(1)	0.5 (3)	$(30^+) \rightarrow (28^+)$		$(E2)$
1150.3 (2)	0.27 (2)	$10^+ \rightarrow 8^+$	1.4 (3)	$E2$
1188^t(1)	0.1 (1)	$(31^-) \rightarrow (29^-)$		$(E2)$
1230 (1)	0.5 (2)	$(28^+) \rightarrow (26^+)$		$(E2)$
1251^t(1)	0.2 (1)	$(32^+) \rightarrow (30^+)$		$(E2)$
1291 (1)	0.2 (1)	$(8^+) \rightarrow 6^+$		$(E2)$
1325^t(1)	0.3 (2)	$(30^+) \rightarrow (28^+)$		$(E2)$

TABLE III. Properties of γ-ray transitions in ^{125}Ce. The intensities, given in the second column from the left, are normalized to the intensity of the 134.7-keV ($9/2^- \rightarrow 7/2^-$) transition having an arbitrary 100 units. The given multipolarities are inferred from the angular-intensity ratios R_θ and from systematics. The angular-intensity ratios marked by a superscript letter *c* are values for a composite peak. The spins and multipolarities in parentheses are tentative. The transitions with energies marked by a superscript letter *t* are placed tentatively in the level scheme. Those marked by a superscript letter *a* belong to Band 4, which is not definitively linked to Bands 2 and 3. The relative spins of Bands 2 and 3, and Band 4 are therefore estimated, but it is unlikely that the estimates will be wrong by more than $4\hbar$.

E_γ (keV)	I_γ (%)	$I_i^\pi \rightarrow I_f^\pi$	R_θ	Multipolarity
56		$9/2^+ \rightarrow 7/2^+$		($M1$)
79		$13/2^+ \rightarrow 11/2^+$		($M1$)
103		$17/2^+ \rightarrow 15/2^+$		($M1$)
118		$21/2^+ \rightarrow 19/2^+$		($M1$)
132		$25/2^+ \rightarrow 23/2^+$		($M1$)
134.7 (2)	100 (1)	$9/2^- \rightarrow 7/2^-$	0.81 (2)	$M1$
135.2 (2)	100 (3)	$7/2^+ \rightarrow 5/2^+$	0.74 (3)	$M1$
147.1 (2)	64 (2)	$9/2^+ \rightarrow 7/2^+$	0.86 (2)	$M1$
150.3 (2)	14 (5)	$7/2^+ \rightarrow 5/2^+$	1.6 (2)	($M1$)
166.8 (2)	68.5 (8)	$11/2^- \rightarrow 9/2^-$	0.80 (1)	$M1$
173.3 (2)	6 (2)	$7/2^+ \rightarrow 3/2^+$		($E2$)
180.9 (2)	53 (2)	$11/2^+ \rightarrow 9/2^+$	0.76 (1)	$M1$
187.2 (2)	7 (1)	$9/2^+ \rightarrow 7/2^+$	0.60 (1)	$M1$
198.4 (2)	30 (4)	$13/2^+ \rightarrow 11/2^+$	0.64 (2)	$M1$
206.3 (2)	13.5 (5)	$9/2^+ \rightarrow 5/2^+$	1.45 (3)	$E2$
211.5 (2)	46.6 (7)	$13/2^- \rightarrow 11/2^-$	0.77 (1)	$M1$
216.1 (2)	13.2 (9)	$13/2^+ \rightarrow 11/2^+$	0.72 (2)	$M1$
216.3 (2)	2.2 (3)	$17/2^+ \rightarrow 15/2^+$	0.71 (2)	$M1$
224.9 (2)	23.9 (5)	$15/2^- \rightarrow 13/2^-$	0.76 (2)	$M1$
233.8 (2)	6.2 (6)	$15/2^+ \rightarrow 13/2^+$	0.75 (4)	$M1$
259.2 (2)	4.4 (3)	$11/2^+ \rightarrow 9/2^+$	1.42 (7)	($M1$)
263.3 (2)	2.9 (3)	$31/2^- \rightarrow 29/2^-$	0.76 (1)	$M1$
265.6 (2)	20.2 (7)	$19/2^- \rightarrow 17/2^-$	0.76 (1)	$M1$
269.4 (2)	8.3 (6)	$17/2^+ \rightarrow 15/2^+$	0.79 (5)	$M1$
282.8 (2)	4.5 (5)	$19/2^+ \rightarrow 17/2^+$	0.79 (5)	$M1$
283.0 (2)	9 (1)	$9/2^+ \rightarrow 5/2^+$	1.40 (9)	$E2$
288.3 (2)	3.1 (3)	$27/2^- \rightarrow 25/2^-$	0.73 (3)	$M1$
289.7 (2)	8.9 (4)	$23/2^- \rightarrow 21/2^-$	0.74(1)^c	$M1$
289.8 (2)	21.1 (8)	$17/2^- \rightarrow 15/2^-$	0.74(1)^c	$M1$
301.2 (2)	16.3 (4)	$11/2^- \rightarrow 7/2^-$	1.35 (3)	$E2$
315.0 (2)	2.1 (2)	$21/2^+ \rightarrow 19/2^+$		($M1$)
315.4 (2)	6 (2)	$11/2^+ \rightarrow 7/2^+$	1.36 (4)	$E2$
318 (1)	10.0 (3)	$35/2^- \rightarrow 33/2^-$	0.73 (3)	$M1$
320.3 (2)	8.3 (5)	$23/2^+ \rightarrow 21/2^+$	0.70 (2)	$M1$
327.4 (2)	10.7 (9)	$11/2^+ \rightarrow 7/2^+$	1.7 (1)	$E2$
335.8 (2)	4.2 (4)	$27/2^+ \rightarrow 25/2^+$		($M1$)
337.8^a(2)	6.5 (2)	$(15/2^+) \rightarrow (11/2^+)$		($E2$)
338.6 (2)	20.6 (7)	$13/2^+ \rightarrow 9/2^+$	1.37 (2)	$E2$
350.3 (2)	2.7 (3)	$25/2^+ \rightarrow 23/2^+$	0.66 (3)	$M1$
350.6 (2)	13.0 (3)	$33/2^- \rightarrow 31/2^-$	0.74 (1)	$M1$
362.3 (2)	2.1 (2)	$15/2^+ \rightarrow 13/2^+$	1.37 (6)	($M1$)
364.5 (2)	7.8 (2)	$21/2^- \rightarrow 19/2^-$	0.74 (3)	$M1$

TABLE III. (*Continued.*)

E_γ (keV)	I_γ (%)	$I_i^\pi \rightarrow I_f^\pi$	R_θ	Multipolarity
377.1 (2)	12.4 (4)	$13/2^- \rightarrow 9/2^-$	1.40 (3)	*E*2
379.5 (2)	14 (1)	$13/2^+ \rightarrow 9/2^+$	1.42 (4)	*E*2
390.2 (2)	5.6 (5)	$37/2^- \rightarrow 35/2^-$	0.75 (3)	*M*1
393.2 (2)	4.2 (6)	$39/2^- \rightarrow 37/2^-$	0.74 (7)	*M*1
396.6 (2)	16.0 (7)	$13/2^+ \rightarrow 9/2^+$	1.43 (8)	*E*2
397.1 (2)	10.8 (3)	$29/2^- \rightarrow 27/2^-$	0.75 (4)	*M*1
408.7 (2)		$(31/2^+) \rightarrow 29/2^+$		(*M*1)
421.7 (2)	10.0 (4)	$25/2^- \rightarrow 23/2^-$	0.75 (3)	*M*1
433.9 (2)		$(35/2^+) \rightarrow 33/2^+$		(*M*1)
435.9 (2)	39.1 (6)	$15/2^- \rightarrow 11/2^-$	1.26 (2)	*E*2
441.2 (2)	9 (4)	$15/2^+ \rightarrow 11/2^+$	1.49 (3)	*E*2
444.4 (2)	2.1 (2)	$19/2^+ \rightarrow 17/2^+$	1.30 (3)	(*M*1)
446.5 (2)	6.4 (8)	$17/2^+ \rightarrow 13/2^+$	1.30 (3)	*E*2
447.3[a](2)	4.7 (4)	$(19/2^+) \rightarrow (15/2^+)$		(*E*2)
449.1 (2)	2.8 (4)	$41/2^- \rightarrow 39/2^-$		(*M*1)
449.3 (2)	16.9 (8)	$15/2^+ \rightarrow 11/2^+$	1.23 (4)	*E*2
460.9 (2)	3.6 (4)	$43/2^- \rightarrow 41/2^-$		(*M*1)
465.3 (2)	27.4 (8)	$17/2^+ \rightarrow 13/2^+$	1.29 (3)	*E*2
501 (1)		$23/2^+ \rightarrow 21/2^+$		(*M*1)
503.4 (2)	14.2 (8)	$17/2^+ \rightarrow 13/2^+$	1.49 (7)	*E*2
514.6 (2)	21.8 (4)	$17/2^- \rightarrow 13/2^-$	1.23 (3)	*E*2
519.2 (9)		$45/2^- \rightarrow 43/2^-$		(*M*1)
546.7 (2)	7 (3)	$19/2^+ \rightarrow 15/2^+$	1.58 (4)	*E*2
549.0[a](2)	4.2 (5)	$(23/2^+) \rightarrow (19/2^+)$	1.23 (5)	*E*2
550.3[a](2)	4.2 (5)	$(27/2^+) \rightarrow (23/2^+)$	1.23 (5)	*E*2
551.3 (2)	3.2 (3)	$31/2^+ \rightarrow 27/2^+$	1.43 (5)	*E*2
554.4 (2)	22 (1)	$19/2^+ \rightarrow 15/2^+$	1.27 (4)	*E*2
555.6 (2)	40.9 (6)	$19/2^- \rightarrow 15/2^-$	1.47 (2)	*E*2
562.2 (2)	26 (2)	$21/2^+ \rightarrow 17/2^+$	1.38 (2)	*E*2
569 (1)	7 (2)	$(31/2^+) \rightarrow 27/2^+$	1.56 (4)	*E*2
592.1 (2)	4 (1)	$(31/2^+) \rightarrow 27/2^+$		(*E*2)
600.2 (2)	6.0 (5)	$21/2^+ \rightarrow 17/2^+$	1.46 (9)	*E*2
612.9 (2)	12 (2)	$33/2^- \rightarrow 29/2^-$	1.26 (3)	*E*2
613.3 (2)	16 (1)	$33/2^+ \rightarrow 29/2^+$	1.38 (3)	*E*2
620.3 (2)	6 (2)	$23/2^+ \rightarrow 19/2^+$	1.31 (5)	*E*2
620.4 (2)	4 (2)	$27/2^+ \rightarrow 23/2^+$	1.31 (5)	*E*2
631.2 (2)	21.7 (4)	$21/2^- \rightarrow 17/2^-$	1.51 (3)	*E*2
633.7 (2)	24 (2)	$25/2^+ \rightarrow 21/2^+$	1.41 (2)	*E*2
634.7 (2)	9 (3)	$23/2^+ \rightarrow 19/2^+$	1.41 (3)	*E*2
637.2 (2)	6 (2)	$(35/2^+) \rightarrow (31/2^+)$		(*E*2)
647.3 (2)	21 (2)	$29/2^+ \rightarrow 25/2^+$	1.48 (3)	*E*2
652.4[a](2)	4.1 (2)	$(31/2^+) \rightarrow (27/2^+)$		(*E*2)
654.2 (2)	16 (1)	$37/2^+ \rightarrow 33/2^+$	1.34 (3)	*E*2
654.4 (2)	38 (1)	$23/2^- \rightarrow 19/2^-$	1.54 (2)	*E*2
659.8 (2)	27.9 (9)	$31/2^- \rightarrow 27/2^-$	1.54 (2)	*E*2
668.7 (2)	18.3 (4)	$35/2^- \rightarrow 31/2^-$	1.34 (4)	*E*2
670.3 (2)	14.4 (8)	$25/2^+ \rightarrow 21/2^+$	1.24 (5)	*E*2
671.1 (2)	2.0 (4)	$35/2^+ \rightarrow 31/2^+$	1.70 (5)	*E*2

TABLE III. (*Continued.*)

E_γ (keV)	I_γ (%)	$I_i^\pi \rightarrow I_f^\pi$	R_θ	Multipolarity
685.2 (2)	14.2 (3)	$29/2^- \rightarrow 25/2^-$	1.70 (4)	*E*2
685.3 (2)	10.1 (8)	$27/2^+ \rightarrow 23/2^+$	1.39 (5)	*E*2
686 (1)	14.2 (3)	$(33/2^+) \rightarrow (29/2^+)$	1.39 (5)	*E*2
702 (1)	9.3 (6)	$(37/2^+) \rightarrow (33/2^+)$		(*E*2)
707.4 (2)	11 (1)	$37/2^- \rightarrow 33/2^-$	1.34 (1)	*E*2
710.3 (2)	34 (3)	$27/2^- \rightarrow 23/2^-$	1.34 (1)	*E*2
711.8 (2)	18 (1)	$25/2^- \rightarrow 21/2^-$	1.34 (1)	*E*2
724.3[a](2)	3.2 (5)	$(35/2^+) \rightarrow (31/2^+)$		(*E*2)
736 (1)	2.7 (5)	$(39/2^+) \rightarrow (35/2^+)$	1.69 (9)	*E*2
743.4 (2)	13 (1)	$41/2^+ \rightarrow 37/2^+$	1.23 (3)	*E*2
744 (1)	16 (2)	$(29/2^+) \rightarrow 25/2^+$		(*E*2)
770[a](1)	1.4 (5)	$(43/2^+) \rightarrow (39/2^+)$		(*E*2)
772.1 (2)	1.2 (3)	$(39/2^+) \rightarrow 35/2^+$		(*E*2)
782.2[a](2)	2.3 (5)	$(39/2^+) \rightarrow (35/2^+)$		(*E*2)
783.1 (2)	12 (2)	$39/2^- \rightarrow 35/2^-$	1.56 (5)	*E*2
798 (1)	7.2 (5)	$(41/2^+) \rightarrow (37/2^+)$		(*E*2)
804[a](2)	0.8 (3)	$(47/2^+) \rightarrow (43/2^+)$		(*E*2)
838 (1)	3.1 (5)	$(43/2^+) \rightarrow (39/2^+)$	1.5 (1)	*E*2
841.0 (2)	8.0 (3)	$41/2^- \rightarrow 37/2^-$	1.53 (7)	*E*2
843.4 (2)	9.1 (9)	$45/2^+ \rightarrow 41/2^+$	1.54 (4)	*E*2
856 (1)	3.3 (5)	$(35/2^-) \rightarrow (31/2^-)$		(*E*2)
858 (1)	1.2 (8)	$(43/2^+) \rightarrow (39/2^+)$		(*E*2)
888 (1)	4 (1)	$(45/2^+) \rightarrow (41/2^+)$		(*E*2)
888[a](1)	0.5 (1)	$(51/2^+) \rightarrow (47/2^+)$		(*E*2)
910.4 (2)	9.0 (3)	$43/2^- \rightarrow 39/2^-$	1.51 (5)	*E*2
933 (1)	3.5 (5)	$(47/2^+) \rightarrow (43/2^+)$	1.4 (1)	*E*2
934 (1)	1.0 (4)	$(47/2^+) \rightarrow (43/2^+)$		(*E*2)
947.2 (2)	4.5 (6)	$49/2^+ \rightarrow 45/2^+$	1.34 (4)	*E*2
960[a](1)	0.3 (1)	$(55/2^+) \rightarrow (51/2^+)$		(*E*2)
976 (1)	2.8 (4)	$(49/2^+) \rightarrow (45/2^+)$		(*E*2)
980.4 (2)	7.8 (4)	$45/2^- \rightarrow 41/2^-$	1.43 (7)	*E*2
1016 (1)	6.4 (4)	$(31/2^-) \rightarrow 27/2^-$		(*E*2)
1016 (1)	3.2 (4)	$(51/2^+) \rightarrow (47/2^+)$	1.7 (3)	*E*2
1019 (1)	0.8 (2)	$(51/2^+) \rightarrow (47/2^+)$		(*E*2)
1031[a,t](1)	0.20 (5)	$(59/2^+) \rightarrow (55/2^+)$		(*E*2)
1035 (1)	8 (1)	$(47/2^-) \rightarrow 43/2^-$	1.39 (7)	*E*2
1049 (1)	3.9 (5)	$53/2^+ \rightarrow 49/2^+$	1.39 (7)	*E*2
1067 (1)	2.5 (5)	$(53/2^+) \rightarrow (49/2^+)$		(*E*2)
1094 (1)	2.3 (4)	$(55/2^+) \rightarrow (51/2^+)$		(*E*2)
1115 (1)	0.6 (2)	$(55/2^+) \rightarrow (51/2^+)$		(*E*2)
1118 (1)	6.5 (5)	$(49/2^-) \rightarrow 45/2^-$		(*E*2)
1145 (1)	7.1 (5)	$(51/2^-) \rightarrow (47/2^-)$		(*E*2)
1149 (1)	2.3 (4)	$(57/2^+) \rightarrow 53/2^+$		(*E*2)
1167 (1)	2.2 (5)	$(57/2^+) \rightarrow (53/2^+)$		(*E*2)
1175 (1)	0.6 (2)	$(59/2^+) \rightarrow (55/2^+)$		(*E*2)
1214 (1)	0.5 (1)	$(59/2^+) \rightarrow (55/2^+)$		(*E*2)
1227 (1)	5 (1)	$(55/2^-) \rightarrow (51/2^-)$		(*E*2)
1241 (1)	1.8 (6)	$(61/2^+) \rightarrow (57/2^+)$		(*E*2)

TABLE III. (*Continued.*)

E_γ (keV)	I_γ (%)	$I_i^\pi \rightarrow I_f^\pi$	R_θ	Multipolarity
1248 (1)	5 (1)	$(53/2^-) \rightarrow (49/2^-)$		$(E2)$
1255 (1)	2.0 (5)	$(63/2^+) \rightarrow (59/2^+)$		$(E2)$
1260 (1)	2.0 (5)	$(61/2^+) \rightarrow (57/2^+)$		$(E2)$
1312 (1)	0.3 (1)	$(63/2^+) \rightarrow (59/2^+)$		$(E2)$
1316 (1)	1.4 (4)	$(67/2^+) \rightarrow (63/2^+)$		$(E2)$
1328 (1)	1.3 (5)	$(65/2^+) \rightarrow (61/2^+)$		$(E2)$
1328^t (1)	0.9 (5)	$(71/2^+) \rightarrow (67/2^+)$		$(E2)$
1332^t (1)	3.0 (5)	$(57/2^-) \rightarrow (53/2^-)$		$(E2)$
1360^t (1)	0.6 (2)	$(75/2^+) \rightarrow (71/2^+)$		$(E2)$
1363^t (1)	2.0 (5)	$(65/2^+) \rightarrow (61/2^+)$		$(E2)$
1370^t (1)	0.9 (5)	$(59/2^-) \rightarrow (55/2^-)$		$(E2)$
1397^t (1)	1.5 (5)	$(61/2^-) \rightarrow (57/2^-)$		$(E2)$
1408^t (1)	0.2 (1)	$(67/2^+) \rightarrow (63/2^+)$		$(E2)$
1412^t (1)	1.2 (4)	$(69/2^+) \rightarrow (65/2^+)$		$(E2)$
1495^t (1)	0.8 (4)	$(73/2^+) \rightarrow (69/2^+)$		$(E2)$

of the 409-keV and 434-keV transitions precluded measurement of their R_θ values, it is likely that they are $M1/E2$ transitions. The R_θ values of the transitions linking Band 2 and Band 3 suggest that Bands 2 and 3 have the same parity.

It should be pointed out that the measured R_θ values for some of the interband transitions in Band 3 are not what would be expected for stretched dipole transitions. The 150.3-keV, 259.2-keV, 137.6-keV, and 444.4-keV transitions all have R_θ values around 1.4, characteristic of stretched-quadrupole transitions. The characteristic band structure implies that the transitions must have $M1/E2$ character, and the R_θ values implies that they are strongly mixed.

Band 4 is a decoupled sequence of $\Delta I=2$ transitions. No definite linking transitions could be identified between Band 4 and the other bands. However, it appears that the band is in coincidence with the lowest transitions (150 and 173 keV) of Band 3. On the basis of the decay to Band 3, Band 4 has been tentatively assigned to have positive parity.

It should be noted that there are several differences between the level scheme deduced in this work and that proposed in Ref. [15]. The larger number of counts in the present work enabled the transitions observed in Ref. [15] to be placed in the level scheme with more certainty. Some of the transitions in Band 1 have been rearranged: the 710-keV transition has been placed below the 660-keV transition, the 783-keV transition has been replaced by the 669-keV transition, and the 683-keV transition has been replaced by the 712-keV transition, with the 683-keV and 783-keV transitions being placed higher in the bands. (Difficulty in placing the 712-keV and 710-keV transitions is not surprising: the ~710-keV peak in Fig. 2 represents three transitions at 707, 710, and 712 keV.) In Band 2, the 465-keV transition from Ref. [15] has been replaced by the 503-keV transition; the 465-keV transition has been assigned to belong to Band 3.

In the period since the work described here, and in Ref. [18], was completed, a separate study of ^{125}Ce has been published by Petrache *et al.* in Ref. [16]. In that work, the ^{92}Mo(^{40}Ca, $\alpha 2pn$) reaction was used. Bands 1, 2, and 3 observed in the present work were all observed in their work, but at lower spins; for example, Band 2 was observed up to spin 25/2 in Ref. [16] compared to 75/2 in the present work. Band 4 in the present work was not observed in the work of Ref. [16]. Similarly, Band 4 of Ref. [16] was only very weakly observed in the present data, and was not unambiguously assigned to ^{125}Ce. For that reason, and because no additional information could be obtained from the present data, that band is not presented or discussed here.

The only significant disagreement between the present work and that of Ref. [16] is the multipolarity of the 283-keV transition in Band 2. In the present work, the measured R_θ value suggests that the 283-keV transition has $E2$ character, and it has been assigned to be a member of the rotational sequence. In Ref. [16], the 283-keV transition has been assigned $E1$ multipolarity. This has the consequence of lowering the spins of Bands 2 and 3 in Ref. [16], compared to the present work, which in turn has led to a different configuration assignment for Band 3, to that proposed here. The configuration assignments are discussed in Sec. V.

B. Alignments and Routhians

The aligned angular momenta and Routhians have been extracted from the data using the method described in Ref. [25]. The data were calculated using the spins given in Figs. 6 and 7. As mentioned above, the spins of Band 4 in ^{125}Ce are particularly uncertain, and no discrete transitions have been observed linking Band 4 to Bands 2 and 3. The K and Ω values used are given in Sec. V B. These data for ^{124,125}Ce are plotted against rotational frequency in Figs. 8–10. On these figures, a reference with Harris parameters [26] of $\mathcal{J}_0 = 17.0\ \mathrm{MeV}^{-1}\hbar^2$ and $\mathcal{J}_1 = 25.8\ \mathrm{MeV}^{-3}\hbar^4$ has been subtracted from all data points. These Harris parameters were originally obtained from a fit to the S band in ^{130}Ce [27], and are used here to enable comparison with earlier work on the heavier cerium isotopes.

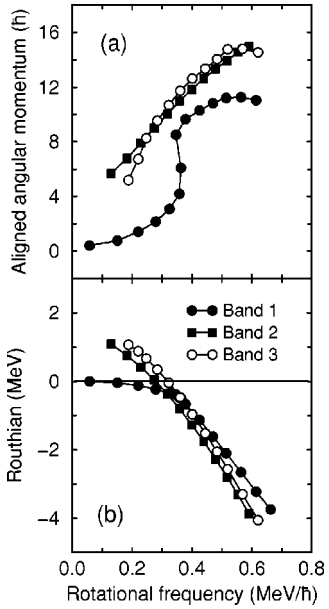

FIG. 8. The (a) aligned angular momenta and (b) Routhians for the three bands in ^{124}Ce. For all data points, a reference with Harris parameters of $\mathcal{J}_0 = 17.0$ MeV$^{-1}\hbar^2$ and $\mathcal{J}_1 = 25.8$ MeV$^{-3}\hbar^4$ has been subtracted.

V. DISCUSSION

A. Total-Routhian surface and cranked Woods-Saxon calculations

Calculations have been performed which predict the high-spin behavior of specific configurations of quasiparticles. From a comparison with experimental data, these calculations assist in assigning quasiparticle configurations of the observed rotational bands. Initially, the total-Routhian surface (TRS) method was used to calculate the deformations of the most likely configurations of quasiparticles in ^{124,125}Ce. The TRS method is described in detail in Refs. [28–31]. In essence, for a given number of quasiparticles with specific parity π and signature α, the total Routhian of the nucleus is minimized with respect to the deformation parameters β_2, β_4, and γ, at steps in rotational frequencies, resulting in a TRS for each frequency. Although each TRS has a well-defined parity and signature, no other quantum numbers are conserved. The likely configurations in ^{124,125}Ce were chosen by determining which orbitals are near the Fermi surface, using predictions from Woods-Saxon calculations, and from a consideration of known configurations in neighboring nuclei, such as ^{124,126}Ba [23,32]. Proton single-particle orbitals from Woods-Saxon calculations are shown in Fig. 11. The deformations of these configurations were then extracted from the TRS calculations. In this work, the standard nomenclature for labeling orbitals has been adopted (see, for example, Ref. [23]); this is summarized in Table IV. The positive-parity orbitals have been labeled with the subshell from which they originate. However, at the deformations involved here, the positive-parity orbitals will be strongly mixed; for example, the $g_{7/2}$ and $d_{5/2}$ orbitals will mix and exchange character.

The deformations extracted from TRS calculations are given in Table V. In order to examine the behavior of the quasiparticle excitations for a particular energy minimum in the TRS, cranked shell model calculations have been performed using the same Woods-Saxon potential [33,34]. In the calculations, the pairing strength was calculated at zero frequency, and decreased with increasing rotational frequency so that it reached 50% of its original value at 0.7 MeV/$\hbar$. This treatment of the pairing is described in detail in Ref. [30]. Typical results of the calculations are shown in Fig. 12; from such quasiparticle diagrams the alignment frequencies of quasiparticle pairs can be extracted. In Fig. 12, the alignment frequencies of the πef, πfg, νEF, and νFG quasiparticle pairs are marked by vertical lines. The alignment frequencies, thus extracted, for the lowest three pairs of negative-parity quasiparticles and the lowest pair of positive-parity quasiparticles, are given in Table VI. The interaction strengths V at the νEF and πef alignments are also indicated in Fig. 12.

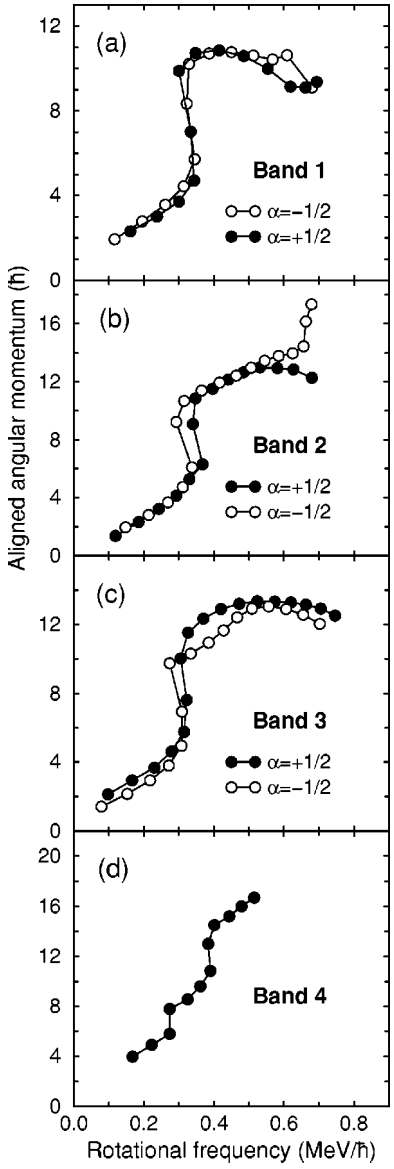

FIG. 9. The aligned angular momenta for the bands in ^{125}Ce. For all data points, a reference with Harris parameters of $\mathcal{J}_0 = 17.0$ MeV$^{-1}\hbar^2$ and $\mathcal{J}_1 = 25.8$ MeV$^{-3}\hbar^4$ has been subtracted.

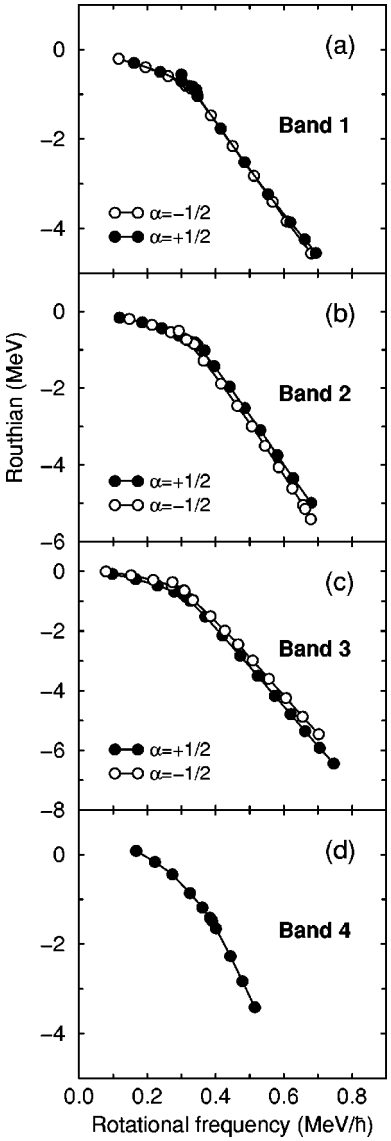

FIG. 10. The Routhians of the bands in ^{125}Ce. For all data points, a reference with Harris parameters of $\mathcal{J}_0=17.0$ MeV$^{-1}\hbar^2$ and $\mathcal{J}_1=25.8$ MeV$^{-3}\hbar^4$ has been subtracted.

The results of the TRS calculations (Table V) reveal that the various expected configurations in ^{124,125}Ce have slightly different deformations. In order to investigate how the calculated alignment frequencies depend on the deformation, cranked shell model (CSM) calculations have been performed where, of the three deformation parameters β_2, β_4, and γ, two are fixed while the third is systematically varied. The results of this study are given in Fig. 13. Over the range of deformations given in Table V ($0.284 \leqslant \beta_2 \leqslant 0.298$, $0.009 \leqslant \beta_4 \leqslant 0.031$, $-6.1° \leqslant \gamma \leqslant 2.1°$) there is very little change in any of the calculated alignment frequencies. For this reason, the alignment frequencies calculated at a representative deformation of $\beta_2=0.292, \beta_4=0.01, \gamma=0°$ are applicable to bands built on all of the likely configurations given in Table V. Furthermore, when the same pairs of quasiparticles are expected to align at the same rotational frequencies in all of the bands, then this simplifies the application and discussion of blocking arguments. These calculated alignment frequencies are given in Table VI, for $Z=58$ and $N=66,67$.

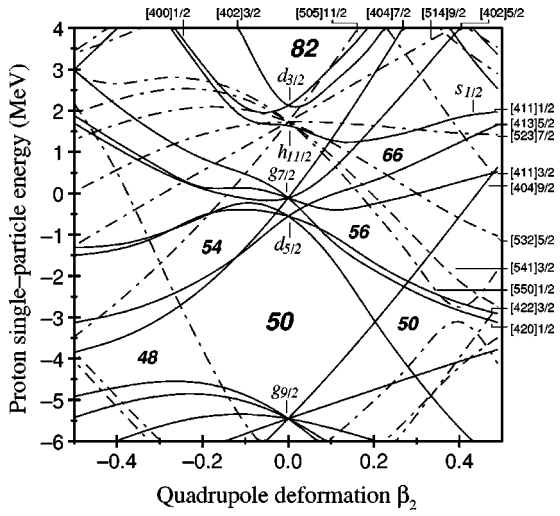

FIG. 11. Woods-Saxon single-particle energy levels for protons. Positive- and negative-parity orbitals are represented by solid and dashed lines, respectively. Several of the orbitals are labeled by the subshell to which they belong (in italics) and by their asymptotic Nilsson quantum numbers (above and to the right of the figure).

B. Configuration assignments

In ^{124}Ce, Band 1 is based on the quasiparticle vacuum at low spins. Band 2 is analogous to negative-parity bands observed in ^{126,128}Ce [2,3,22]. A comparison of these bands, together with a study of the orbitals near the Fermi surface, suggests that the configuration of Band 2 is $\pi(h_{11/2})[541]3/2^- \otimes \pi(g_{7/2})[422]3/2^+$, giving the band $K=3$. Band 3 is, however, more difficult to describe. An inspection of the orbitals near the Fermi surface suggests that $\pi(h_{11/2})[541]3/2^- \otimes \pi(h_{11/2})[550]1/2^-$ (πfg configuration) is a possibility, giving $K=2$.

Previous work has suggested that Band 1 in ^{125}Ce is based on the $\nu(h_{11/2})[523]7/2^-$ orbital, and that Band 2 is based on the $\nu(d_{5/2})[402]5/2^+$ orbital. The discussion given below suggests that Band 3 is based on the $\nu(d_{5/2})[411]3/2^+$ orbital; the experimental observations suggest that this is the most
probable configuration for Band 3, but it should probably be considered less definite than that assigned to Band 2. Band 4 is probably based on one of the $\nu(d_{5/2})[420]1/2^+$ or $\nu(d_{3/2})[411]1/2^+$ orbitals. The experimentally extracted Routhians for all of the bands in ^{125}Ce are shown in Fig. 10. The signature splitting in the ^{125}Ce bands is consistent with these proposed configurations. Band 3 has a larger signature splitting than the other bands, suggesting that the orbital upon which this band is based has a lower value of Ω than the other bands. Since Band 2 has been assigned $\Omega=5/2$, a value of $\Omega=3/2$ or $1/2$ is likely for Band 3, which is consistent with the $[411]3/2^+$ assignment. All of these configurations are consistent with the observed alignment characteristics discussed in the following section.

TABLE IV. Nomenclature for orbitals near the Fermi surface in ^{124,125}Ce, for $\beta_2 \simeq 0.292$.

		Nilsson configuration	Label	
	Subshell	$[Nn_z\Lambda]\Omega^\pi$	$\alpha=-1/2$	$\alpha=+1/2$
Neutrons	$d_{5/2}$	$[402]5/2^+$	B	A
	$d_{5/2}$	$[411]3/2^+$	D	C
	$h_{11/2}$	$[523]7/2^-$	E	F
	$h_{11/2}$	$[532]5/2^-$	G	H
Protons	$d_{5/2}$	$[420]1/2^+$	b	a
	$g_{7/2}$	$[413]5/2^+$	c	d
	$h_{11/2}$	$[541]3/2^-$	e	f
	$h_{11/2}$	$[550]1/2^-$	g	h

C. Quasiparticle alignments

The quasiparticle alignments in ^{124}Ce are most easily understood with reference to the ^{125}Ce alignment data. Therefore, in this section, the discussion of alignments in ^{125}Ce is presented before that of ^{124}Ce.

1. ^{125}Ce

Band 1 has been interpreted to be based on the negative-parity $\nu(h_{11/2})[523]7/2^-$ orbital. This band is therefore expected to exhibit the πef alignment. The aligned angular momentum of Band 1 is shown in Fig. 9(a). The πef alignment, predicted to occur at a rotational frequency of 0.34 MeV/$\hbar$, is observed experimentally as a sharp upbend at $\sim$0.35 MeV/$\hbar$. Both the νEF and νEH alignments would be blocked, and indeed are not observed. Alignments predicted at higher rotational frequencies, such as the νFG alignment at 0.50 MeV/$\hbar$ are not clearly seen.

Band 2 is interpreted to be based on the positive-parity $\nu d_{5/2}[402]5/2^+$ neutron orbital. In this band, neither the νEF nor the πef alignment is blocked, and both should be observed experimentally. The aligned angular momentum of Band 2 is shown in Fig. 9(b). The alignment observed at 0.35 MeV/$\hbar$ is in good agreement with the πef alignment, predicted at 0.34 MeV/$\hbar$. Above the first alignment, a more gradual gain in aligned angular momentum is observed, which can be interpreted as the νEF alignment, centered around a rotational frequency of about 0.42 MeV/$\hbar$. The gradual nature of this second alignment suggests that the interaction strength is larger than that of the πef alignment. A second clear upbend is observed at 0.7 MeV/$\hbar$ in the $\alpha=-1/2$ signature of Band 2. This upbend would be a candidate for the alignment of the first pair of positive-parity quasiparticles. However, as the upbend involves tentative transi-

TABLE V. Deformations of configurations in ^{124,125}Ce, extracted from TRS calculations. In the two columns on the left-hand side, the symbol and figure in parentheses represent (π,α), where π is the parity and α is the signature quantum number. The value of ω was taken to be just below the first quasiparticle alignment in each case.

ν (π,α)	π (π,α)	ω MeV/$\hbar$	β_2	β_4	γ (deg)
		^{124}Ce			
Vacuum	Vacuum	0.187	0.298	0.025	−1.4
Vacuum	ef(+,0)	0.187	0.287	0.019	0.9
Vacuum	fg(+,0)	0.187	0.291	0.020	2.1
EF(+,0)	Vacuum	0.187	0.284	0.011	−2.5
Vacuum	eb(−,1)	0.187	0.292	0.031	−6.1
		^{125}Ce			
E(−,−1/2)	Vacuum	0.186	0.289	0.009	−1.1
F(−,+1/2)	Vacuum	0.186	0.289	0.009	−0.8
A(+,+1/2)	Vacuum	0.186	0.295	0.014	−0.7
B(+,−1/2)	Vacuum	0.186	0.294	0.011	−0.5

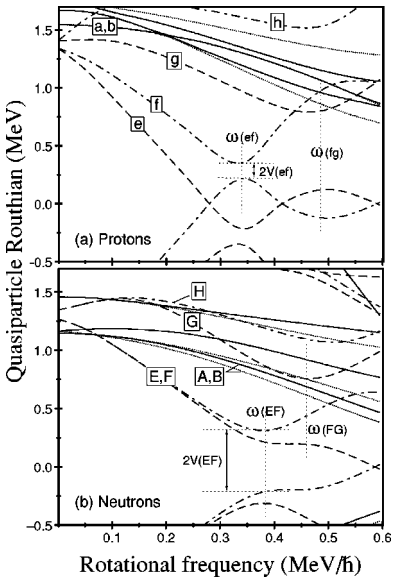

FIG. 12. Quasiparticle Routhians for (a) protons at $Z=58$ and (b) neutrons at $N=66$. The Routhians are calculated with the deformation parameters $\beta_2=0.292$, $\beta_4=0.01$, and $\gamma=0°$. The parity and signature quantum numbers (π,α) of each quasiparticle trajectory are given by the style of the lines: $(+,+1/2)$ is represented by solid lines; $(+,-1/2)$ by dotted lines; $(-,-1/2)$ by dashed lines; and $(-,+1/2)$ by dot-dashed lines. The frequencies of the πef, πfg, νEF, and νFG quasiparticle alignments are shown by the vertical dotted lines. The interaction strengths V at the πef and νEF alignments are indicated.

TABLE VI. Calculated alignment frequencies, in MeV/$\hbar$, for $\beta_2=0.292, \beta_4=0.01$, and $\gamma=0°$.

Protons	Neutrons	
$Z=58$	$N=66$	$N=67$
$\omega(\mathrm{ef})=0.34$	$\omega(\mathrm{EF})=0.39$	$\omega(\mathrm{EF})=0.39$
$\omega(\mathrm{fg})=0.48$	$\omega(\mathrm{FG})=0.48$	$\omega(\mathrm{FG})=0.50$
$\omega(\mathrm{eh})=0.52$	$\omega(\mathrm{EH})=0.54$	$\omega(\mathrm{EH})=0.60$
$\omega(\mathrm{ab})>0.6$	$\omega(\mathrm{AB})>0.6$	$\omega(\mathrm{AB})>0.6$

tions, no conclusions can be drawn. An alignment plot for Band 3 is shown in Fig. 9(c). The general trends are the same as in Band 2, suggesting that Band 3 also undergoes both the πef and νEF alignments, at about 0.35 and 0.42 MeV/$\hbar$, respectively. This is consistent with the $\nu(d_{5/2})[411]3/2^+$ assignment for Band 3.

Additional evidence for the νEF alignment is shown in panel (a) of Fig. 14, where the aligned angular momentum of Band 3 of ^{125}Ce is compared to that of bands in the $Z=57$ neighbor ^{123}La [35]. In the $\pi h_{11/2}$ band of ^{123}La, the πef alignment is blocked, and the gain in aligned angular momentum is due entirely to the alignment of the νEF pair. In the $\pi g_{7/2}$ band of ^{123}La, neither the πef nor the νEF alignment is blocked and both are observed. (The πef alignment occurs early, for reasons discussed in Ref. [35].) The overall alignment gain for ^{125}Ce Band 3, and therefore, using the comparison in Fig. 15, also for Band 2, is the same as that for the $\pi g_{7/2}$ band in ^{123}La. Furthermore, two bands in ^{124}La (not shown in the figures) exhibit the νEF alignment [36] with the same general features (alignment frequency, and gradient of alignment plot) as that proposed to be the νEF alignment in ^{125}Ce.

The aligned angular momentum in Band 4 is shown in Fig. 9(d). Alignments are observed at 0.27 and 0.39 MeV/$\hbar$. The lack of similar bands in the neighboring nuclei and the lack of definite linking transitions make it difficult to assign a configuration to Band 4. The decoupled nature of

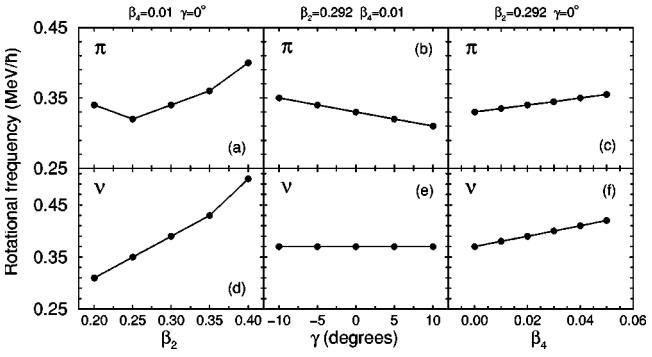

FIG. 13. Frequencies of the πef and νEF alignments extracted from cranked shell model calculations. The upper panels give the alignment frequencies of pairs of $h_{11/2}$ protons (πef) plotted against (a) β_2, (b) γ, and (c) β_4. The lower panels give the alignment frequencies of pairs of $h_{11/2}$ neutrons (νEF) plotted against (d) β_2, (e) γ, and (f) β_4. Apart from the parameter being varied, the deformation parameters are fixed at $\beta_2=0.292$, $\beta_4=0.01$, and $\gamma=0°$.

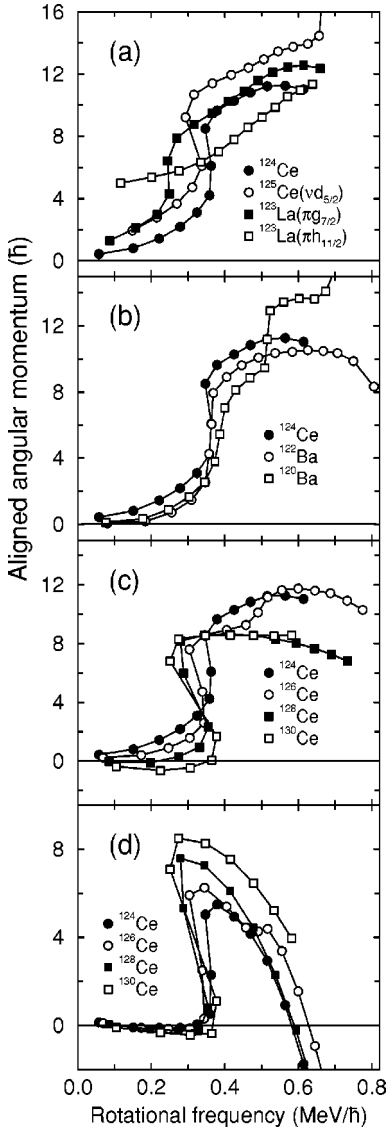

FIG. 14. A comparison of the aligned angular momenta in ^{124}Ce Band 1 with various neighboring nuclei, indicated by the legends. For all data points on panels (a), (b), and (c), a reference with Harris parameters of $\mathcal{J}_0=17.0$ MeV$^{-1}\hbar^2$ and $\mathcal{J}_1=25.8$ MeV$^{-3}\hbar^4$ has been subtracted. For the data in panel (d) the following Harris parameters were used ($\mathcal{J}_0$ in MeV$^{-1}\hbar^2$ and $\mathcal{J}_1$ in MeV$^{-3}\hbar^4$): ^{124}Ce, 22.0 and 67.8; ^{126}Ce, 18.6 and 68.6; ^{128}Ce, 15.7 and 68.9; and ^{124}Ce, 13.8 and 58.6.

Band 4 implies that it could be built on either of the $(d_{3/2})[411]1/2^+$ or $(d_{5/2})[420]1/2^+$ orbitals. In either case both πef and νEF alignments would be observed. The nature of the observed alignments is not clear.

2. ^{124}Ce

The aligned angular momentum for Band 1 in ^{124}Ce is shown in Fig. 8(a). An alignment is observed in Band 1 at 0.34 MeV/$\hbar$. Alignments are also observed at this frequency in the yrast bands of the neighboring barium isotone ^{122}Ba [24] and in ^{120}Ba [37], but not in the yrast $\pi(h_{11/2})$ band of the odd-Z isotone ^{123}La: alignment data for these nuclei are

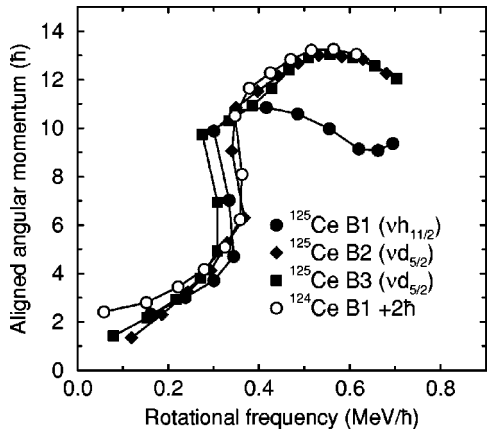

FIG. 15. Comparison of the aligned angular momenta of Band 1 in ^{124}Ce with Band 1 ($\alpha=-1/2$), Band 2 ($\alpha=+1/2$), and Band 3 ($\alpha=+1/2$) in ^{125}Ce. The data for ^{124}Ce have an offset of $2\hbar$ in aligned angular momentum, in order to highlight the similarity of that band and Bands 2 and 3 in ^{125}Ce. For all data points, a reference with Harris parameters of $\mathcal{J}_0=17.0$ MeV$^{-1}\hbar^2$ and $\mathcal{J}_1=25.8$ MeV$^{-3}\hbar^4$ has been subtracted.

compared to Band 1 in panels (a) and (b) of Fig. 14. CSM calculations predict the πef alignment in ^{124}Ce to occur at a rotational frequency of 0.34 MeV/$\hbar$. The first alignment in the yrast bands of ^{120,122}Ba has been interpreted as the πef alignment: this is blocked in the $\pi h_{11/2}$ band of ^{123}La. By comparison with the data for neighboring nuclei and with CSM predictions, it is likely that the alignment in ^{124}Ce can also be attributed to the πef quasiparticles.

The CSM calculations also predict that the νEF alignment will occur at 0.39 MeV/$\hbar$ in ^{124}Ce; experimentally this alignment is not clear. In order to investigate whether the νEF alignment occurs in Band 1, the aligned angular momentum of Band 1 is shown in Fig. 15, in comparison with one of the $\Delta I=2$ sequences from each of Bands 1, 2, and 3 in ^{125}Ce. Bands 2 and 3 of ^{125}Ce are expected to exhibit both the πef and νEF alignments, but in ^{125}Ce Band 1, the νEF alignment will be blocked. This is in agreement with what is observed experimentally; Band 1 of ^{125}Ce has a smaller alignment gain than the other three bands shown. The alignment plot for Band 1 in ^{124}Ce has the same gain and the same general shape as Bands 2 and 3 in ^{125}Ce, where both πef and νEF alignments occur. All three of these bands have a larger total alignment gain than ^{125}Ce Band 1 where only the πef alignment occurs. This comparison therefore suggests that the νEF alignment also occurs in ^{124}Ce Band 1.

The aligned angular momentum for Band 2 in ^{124}Ce is also shown in Fig. 8. This band exhibits a gradual increase in aligned angular momentum over the observed frequency range. The increase in aligned angular momentum at about 0.4 MeV/$\hbar$ in Band 1, from the above discussion, is presumably due to the νEF pair, and it is likely that the increase in aligned angular momentum in Band 2 has the same origin. The observation of the νEF alignment is consistent with the band having the $\pi(h_{11/2})[541]3/2^-\otimes\pi(g_{7/2})[422]3/2^+$ configuration. Band 3, also shown in Fig. 8, exhibits similar alignment characteristics to Band 2. Like Band 2, the gradual increase in alignment can be attributed to the νEF alignment, consistent with the $\pi(h_{11/2})[541]3/2^-\otimes\pi(h_{11/2})[550]1/2^-(\pi\mathrm{fg})$ assignment. Given the above assigned configurations for Band 2 and 3, the πfg and πeh alignments should be observed in the bands, respectively. In the present data there is no obvious sign of these alignments, although it is possible that the gradual rise in alignment in Bands 2 and 3 is due to both νEF and πfg, or νEF and πeh alignments, respectively. The curved shape of the alignment plot for Band 3 is similar to the shape of that for one of the positive-parity bands in ^{128}Ce [3]. For the band in ^{128}Ce, two possible configurations are suggested; either πfg, as above, or a triaxial $\nu(h_{11/2})^2$ band. For ^{128}Ce, TRS calculations predict a secondary triaxial minimum with $\beta_2=0.25$ and $\gamma\simeq-40°$. This triaxial minimum does not appear in the calculations for ^{124}Ce, ruling out this possibility.

3. Systematics of the νEF alignment in $A\leqslant130$ even-even cerium isotopes

In the yrast band of ^{128}Ce, the νEF alignment is not observed: it has been reported that this alignment is delayed by >0.2 MeV/$\hbar$ or is absent [3]. This has been put forward as an inconsistency between the cranked shell model and experimental data with no definite explanation. The alignment systematics for the even-even cerium isotopes with $124\leqslant A\leqslant130$ are shown in panel (c) of Fig. 14; a common Harris-parametrized reference has been subtracted for all of the data. The πef alignments are observed in each of the nuclei shown at about 0.35 MeV/$\hbar$, with the interaction strength increasing with decreasing neutron number: the shape of the πef alignment changes from a clear backbend in ^{130}Ce to a gradual upbend in ^{124}Ce. However, the νEF alignments are not so easy to describe. The interaction strengths and frequencies of the νEF alignments for $^{122-130}$Ce, calculated by the CSM, are shown in Fig. 16. The νEF alignment is not clear for any of the isotopes shown in Fig. 14. The isotope ^{126}Ce differs from the other nuclei, in that an upbend is seen at 0.5 MeV/$\hbar$. In Ref. [2] this is interpreted as the νEF alignment, delayed by 0.1 MeV/$\hbar$ with respect to the CSM-predicted value. The overall gain in alignment in ^{124}Ce and ^{126}Ce, over the observed range in spins, is very similar and is larger than the gain in ^{128}Ce and ^{130}Ce, which suggests that the same alignments occur in both ^{124,126}Ce. However, the second alignment in ^{124}Ce is less distinct, presumably due to a larger interaction strength. The relative interaction strengths of the νEF alignments in ^{124,126}Ce are well explained by the CSM. In ^{126}Ce the νEF interaction strength is predicted to be reduced by almost 50% compared to ^{124}Ce [Fig. 16(a)], which explains the distinct upbend in ^{126}Ce. In ^{124}Ce, the second alignment is centered around 0.45 MeV/$\hbar$. If this is the νEF alignment, then it is in reasonable agreement (delayed by only 0.05 MeV/$\hbar$) compared to the predictions of the CSM [Fig. 16(b)].

To further investigate the nonobservation of the νEF alignment in ^{128,130}Ce, the alignment data for the even cerium isotopes have been replotted in Fig. 14(b). For this figure, the reference has been fit for each individual isotope, by performing a Harris parametrization of the ground-state band below the first alignment. This procedure makes the alignment plots nearly flat (and zero) at the lowest frequen-

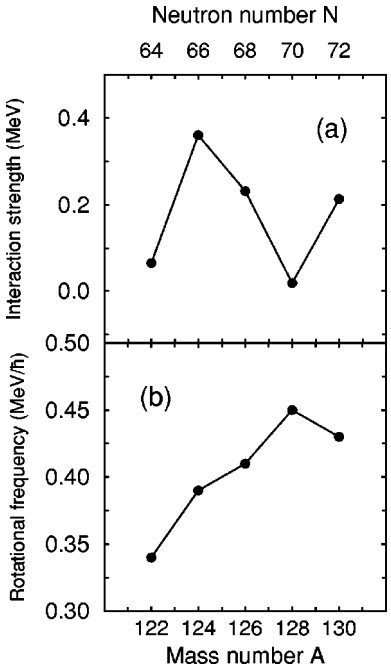

FIG. 16. Properties of the predicted νEF alignments in the even-even cerium isotopes extracted from the cranked shell model calculations. Panel (a) shows interaction strengths and panel (b) shows alignment frequencies, extracted as explained in Ref. [25]. The mass-number and neutron-number scales apply to both panels. The cranked shell model calculations were carried out at the deformations predicted by TRS calculations.

cies, making the details of the first alignment more easily compared. The figure shows that in ^{128,130}Ce, the gain at the first alignment is $3\hbar-4\hbar$ larger than in ^{124,126}Ce. It is therefore plausible that what appears to be the first (πef) alignment in ^{128,130}Ce is, in fact, two alignments: the superposition of both πef and νEF. If this is the case, however, the νEF alignment would have to occur early, at $\sim$0.35 MeV/$\hbar$, which is the opposite behavior to the *delayed* alignments in ^{124,126}Ce, and cannot be explained by cranked shell model calculations.

D. Transition strength ratios

The ratios of the reduced transition probabilities $B(M1)/B(E2)$ can give information about the underlying structure of a rotational band. The values can be strongly dependent upon the occupied orbital and, therefore, a comparison between predictions and experimental values can help to identify the quasiparticle configuration. The experimental $B(M1)/B(E2)$ ratios, in $(\mu_N/e\mathrm{b})^2$, can be extracted from the data using the relation

$$\frac{B(M1;\Delta I=1)}{B(E2;\Delta I=2)} = \frac{0.697}{(1+\delta^2)}\frac{I_\gamma(M1)}{I_\gamma(E2)}\frac{E_\gamma^5(E2)}{E_\gamma^3(M1)}, \qquad (1)$$

where I_γ represents γ-ray intensity and E_γ is the γ-ray energy in units of MeV. In this work, the mixing ratio δ has been assumed to be zero, meaning that the experimental data points are upper limits.

TABLE VII. Summary of parameters used to calculate the Dönau and Frauendorf estimates of $B(M1)/B(E2)$ ratios [38,39] in ^{125}Ce. For each orbital a value of $Q_0=3.58$ eb was used.

Subshell	Nilsson orbital	g_K	i ($\hbar$)	$\Delta e/\hbar\omega$
$\nu(h_{11/2})$	$[532]5/2^-$	−0.21	4.0	0
$\nu(h_{11/2})$	$[523]7/2^-$	−0.21	2.5	0
$\nu(h_{11/2})$	$[514]9/2^-$	−0.21	2.0	0
$\nu(d_{5/2})$	$[402]5/2^+$	−0.46	0	0
$\nu(g_{7/2})$	$[413]5/2^+$	0.26	1.0	0
$\nu(d_{5/2})$	$[411]3/2^+$	−0.46	1.0	100/150

Theoretical estimates for the $B(M1)/B(E2)$ ratios can be obtained from the semiclassical formula of Dönau and Frauendorf [38]. In this work, the formula was used in the form presented in Ref. [39] where

$$\frac{B(M1)}{B(E2)} = \frac{12}{5Q_0^2\cos^2(\gamma+30°)I^2}\left[1-\frac{K^2}{\left(I-\frac{1}{2}\right)^2}\right]^{-2} \times\{(I^2-K^2)^{1/2}A-K(g_K-g_R)i\}^2, \qquad (2)$$

$$A = K(g_K-g_R)\left(1\pm\frac{\Delta e}{\hbar\omega}\right). \qquad (3)$$

In these expressions, the parameter g_R is the rotational gyromagnetic factor, and the standard approximation of $g_R=Z/A$ has been used, which is equal to 0.464 for ^{125}Ce. The g_K parameters are the orbital gyromagnetic factors: for this work, the Schmidt values have been used or the values from the compilation given in Ref. [40] have been used, where possible. The aligned angular momenta i were estimated using the values of j and K for the quasiparticle, where i is $\sqrt{j^2-K^2}$. The values of the quadrupole moments Q_0 were deduced from the deformations given by the TRS calculations. The parameters used in the calculations for ^{125}Ce are summarized in Table VII. The experimental $B(M1)/B(E2)$ values for Bands 1, 2, and 3 in ^{125}Ce are presented in comparison with some of the calculated values, in Fig. 17 and Table VIII. For each band the signature splitting Δe was taken from the observed experimental data.

Before comparing the experimental data points to the calculated values, it is instructive to examine the dependence of the calculated values on the parameters i, Q_0, g_R, and g_K. Figure 18 shows $B(M1)/B(E2)$ values as a function of spin, calculated with different input parameters. On all panels (a)–(d) in Fig. 18, the bold line represents the values calculated with the same input parameters; specifically $i=0$, $Q_0=3.58$ eb, $g_R=0.464$, and $g_K=-0.46$. These values are what would be expected for a neutron in the $\nu(d_{5/2})[402]5/2^+$ orbital. The other curves on each of the panels were calculated by altering the parameters. Panel (a) reveals that changing i by even $1/2\hbar$ can significantly alter the calculated values. Similarly, altering the Q_0 values can have a marked effect, as shown in panel (b). The approximation $g_R=Z/A$ is often modified by a factor of 0.7, to better fit experimental data

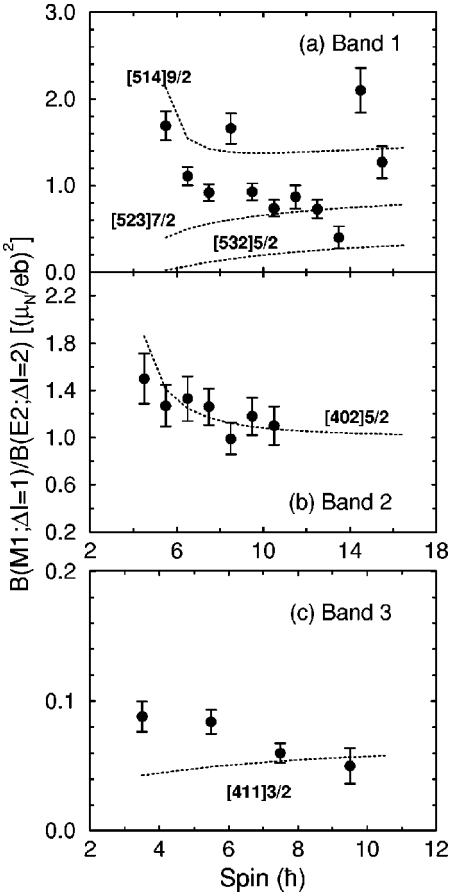

FIG. 17. Experimental $B(M1)/B(E2)$ ratios for the three bands in ^{125}Ce. The uncertainties on the data points are propagated from the uncertainties on the intensities. The dotted lines are calculated using the Dönau and Frauendorf formulas [38,39]. The calculated points are labeled with their Nilsson quantum numbers.

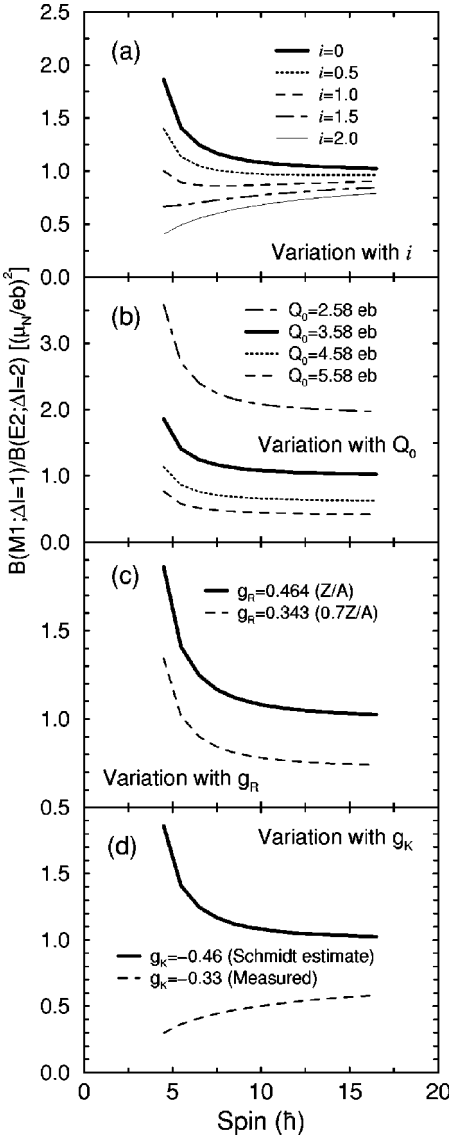

FIG. 18. $B(M1)/B(E2)$ ratios calculated using the formalism of Dönau and Frauendorf. The panels (a), (b), (c), and (d), show how the calculated values vary with i, Q_0, g_R, and g_K, respectively. The bold line represents the same data points on each panel.

[41]; panel (c) illustrates the effect of this alteration on the calculated $B(M1)/B(E2)$ values. Finally, panel (d) shows how the values change when using either the Schmidt estimate of the g_K parameter or the value measured in neighboring nuclei for the $d_{5/2}$ orbital [40].

The $B(M1)/B(E2)$ ratios for Band 1 are shown in Fig. 17(a). The ratios have been measured for all states in Band 1 with spins from $11/2$ to $31/2$. The large errors on some of the data points are due to doublets, or contaminated or weak transitions. The values measured here are in agreement with those measured in Ref. [15], both in magnitude and in overall trend, and average around a value of $1.0(\mu_N/e\mathrm{b})^2$. The discussion of alignments and Routhians, presented earlier and in Ref. [15], suggest that Band 1 is based on the $\nu(h_{11/2})[523]7/2^-$ orbital. Calculated $B(M1)/B(E2)$ values for three $\nu(h_{11/2})$ orbitals in the vicinity of the Fermi surface are shown in Fig. 17(a); the values were calculated using the parameters given in Table VII. The data with the smallest error bars are in best agreement with the calculations for the $\nu(h_{11/2})[523]7/2^-$ orbital, at intermediate and high frequencies. The agreement with any of the calculated orbitals is not very good; however, as pointed out in the preceding paragraphs, the $B(M1)/B(E2)$ ratios are strongly dependent on many parameters. The configuration assignment for Band 1 is more strongly based on the previous work and alignment arguments.

Figure 17(b) shows experimental data for Band 2. For this band, the $B(M1)/B(E2)$ ratios have been measured for all states with spins from $9/2$ to $21/2$. Reference [15] and the earlier discussion suggest that Band 2 is based on the $\nu(d_{5/2})[402]5/2^+$ orbital. The experimental data are in good agreement with the calculations for this orbital.

Finally, Fig. 17(c) shows the experimental values for Band 3. The $B(M1)/B(E2)$ values have been measured for the four states with spins between $7/2$ and $19/2$ in the $\alpha=-1/2$ signature sequence. It was not possible to accurately measure the intensities of the low-energy transitions from the $\alpha=+1/2$ states. As discussed above, it is most likely that this band is based on the $\nu(d_{5/2})[411]3/2^+$ positive-parity orbital. The values calculated for this orbital are shown in Fig. 17(c).

TABLE VIII. Experimentally extracted $B(M1)/B(E2)$ ratios for bands in ^{125}Ce.

Band 1		Band 2		Band 3	
$I(\hbar)$	$B(M1)/B(E2)(\mu_N/eb)^2$	$I(\hbar)$	$B(M1)/B(E2)(\mu_N/eb)^2$	$I(\hbar)$	$B(M1)/B(E2)(\mu_N/eb)^2$
11/2	1.69 (4)	9/2	1.5 (1)	7/2	0.088 (5)
13/2	1.11 (2)	11/2	1.27 (8)	11/2	0.084 (3)
15/2	0.92 (3)	13/2	1.33 (9)	15/2	0.060 (3)
17/2	1.66 (5)	15/2	1.26 (6)	19/2	0.05 (1)
19/2	0.93 (3)	17/2	0.99 (6)		
21/2	0.74 (4)	19/2	1.18 (7)		
23/2	0.87 (7)	21/2	1.10 (8)		
29/2	0.73 (5)				
31/2	0.4 (1)				
33/2	2.1 (1)				
35/2	1.27 (9)				

An approximate value of the signature splitting has been included in the calculations; the calculated points shown are the lower solutions (taking the negative coefficient of Δe in Eq. (2); an examination of how signature splitting affects $B(M1)/B(E2)$ ratios is given in Ref. [38].) The calculated values are in reasonable agreement with the experimental data, although the overall downward trend of the data points is not well reproduced.

VI. SUMMARY AND CONCLUSIONS

In summary, high-spin states have been studied in the very neutron-deficient ^{124,125}Ce isotopes using the Gammasphere γ-ray spectrometer, together with the Microball charged-particle detector array. Despite these isotopes being the most neutron-deficient cerium isotopes studied by γ-ray spectroscopy, their level structures have been extended to over $30\hbar$ above the ground state. Extracted $B(M1)/B(E2)$ ratios are consistent with those calculated for the proposed configurations. Although the dependency on input parameters prevents conclusive comparisons between calculated and extracted $B(M1)/B(E2)$ ratios, consistency can provide supporting evidence when taken in conjunction with other arguments, such as aligned angular momentum and signature splitting.

Alignments of pairs of $h_{11/2}$ neutrons and protons are observed in all of the bands. Generally, the $h_{11/2}$ proton alignments (πef) are in good agreement with the CSM predictions. The $h_{11/2}$ neutron alignments (νEF) agree reasonably well with predictions, although, in the yrast band of ^{124}Ce, the $h_{11/2}$ neutron alignment frequency is delayed by about 0.05 MeV/$\hbar$, with respect to predictions of the CSM. The slight delay of the $h_{11/2}$ neutron alignment in ^{124}Ce is significant, because this alignment has previously been reported to be delayed by 0.1 MeV/$\hbar$ in ^{126}Ce [2] and by $>$0.2 MeV/$\hbar$ in ^{128}Ce [3] (in which case the alignment has not been observed). The interaction strength at the νEF alignment in ^{124}Ce appears larger than that in ^{126}Ce, which is in good agreement with CSM predictions. The apparent ability of the CSM to explain the features of the neutron alignments in ^{124,125}Ce, but not in ^{126,128}Ce is conspicuous, and may indicate a deficiency of the cranked shell model for the localized region near ^{128}Ce, and not a deficiency which increases with decreasing neutron number as implied by the previous ^{128}Ce result.

ACKNOWLEDGMENTS

The authors would like to thank R. Darlington (Daresbury) and A. Lipski (Stony Brook) for target preparation. The CSM and TRS codes were provided by R. Wyss and W. Nazarewicz. This work was supported in part by the NSF, the EPSRC (UK), and by the U.S. Department of Energy, Nuclear Physics Division, under Contract No. W-31-109-ENG-38 (A.N.L.). V.M.C. acknowledges support from La Caixa (Spain) and the British Council.

[1] P. Möller, J. R. Nix, W. D. Myers, and W. J. Swiatecki, At. Data Nucl. Data Tables **59**, 185 (1995).

[2] A. N. Wilson, R. Wadsworth, J. F. Smith, S. J. Freeman, M. Leddy, C. J. Chiara, D. B. Fossan, D. R. LaFosse, K. Starosta, R. V. F. Janssens, M. P. Carpenter, C. N. Davids, D. Seweryniak, M. Devlin, D. G. Sarantites, J. N. Wilson, and R. Wyss, Phys. Rev. C **63**, 054307 (2001).

[3] E. S. Paul, P. Bednarczyk, A. J. Boston, C. J. Chiara, C. Foin, D. B. Fossan, J. Genevey, A. Gizon, J. Gizon, D. G. Jenkins, N. Kelsall, N. Kintz, T. Koike, D. R. LaFosse, P. J. Nolan, B. M. Nyako, C. M. Parry, J. A. Sampson, A. T. Semple, K. Starosta, J. Timár, R. Wadsworth, A. N. Wilson, and L. Zolnai, Nucl. Phys. **A676**, 32 (2000).

[4] L. Grodzins, Phys. Lett. **2**, 88 (1962).

[5] S. Raman, J. A. Sheikh, and K. H. Bhatt, Phys. Rev. C **52**, 1380 (1995).
[6] W. Nazarewicz and I. Ragnarsson, in *Handbook of Nuclear Properties*, edited by D. Poenaru and W. Greiner (Oxford University Press, Oxford, 1996), Chap. 4.
[7] C. J. Lister, B. J. Varley, R. Moscrop, W. Gelletly, P. J. Nolan, D. J. G. Love, P. J. Bishop, A. Kirwan, D. J. Thornley, L. Ying, R. Wadsworth, J. M. O'Donnell, H. G. Price, and A. H. Nelson, Phys. Rev. Lett. **55**, 810 (1985).
[8] K. L. Ying, P. J. Bishop, A. N. James, A. J. Kirwan, D. J. G. Love, T. P. Morrison, P. J. Nolan, D. C. B. Watson, K. A. Connell, A. H. Nelson, and J. Simpson, J. Phys. G **12**, L211 (1986).
[9] P. J. Nolan, F. A. Beck, and D. B. Fossan, Annu. Rev. Nucl. Part. Sci. **44**, 561 (1994).
[10] D. G. Sarantites, P.-H. Hua, M. Devlin, L. G. Sobotka, J. Elson, J. T. Hood, D. R. LaFosse, J. E. Sarantites, and M. R. Maier, Nucl. Instrum. Methods Phys. Res. A **381**, 418 (1996).
[11] A. N. James, T. P. Morrison, P. J. Nolan, D. Watson, K. L. Ying, K. A. Connell, and J. Simpson, Daresbury Laboratory Annual Report No. 198H/198I, 1981, p. 102.
[12] A. N. James, T. P. Morrison, K. L. Ying, K. A. Connell, H. G. Price, and J. Simpson, Nucl. Instrum. Methods Phys. Res. A **267**, 144 (1988).
[13] K. L. Ying, P. J. Bishop, A. N. James, A. J. Kirwan, T. P. Morrison, P. J. Nolan, D. C. B. Watson, K. A. Connell, D. J. G. Love, A. H. Nelson, and J. Simpson, Daresbury Laboratory Annual Report, 1987, p. 27.
[14] A. Osa, M. Asai, M. Koizumi, T. Sekine, S. Ichikawa, Y. Kojima, H. Yamamoto, and K. Kawade, Nucl. Phys. **A588**, 185c (1995).
[15] E. S. Paul, A. J. Boston, A. Galindo-Uribarri, T. N. Ginter, C. J. Gross, A. N. James, P. J. Nolan, R. D. Page, S. D. Paul, A. Piechaczek, D. C. Radford, W. Reviol, L. L. Riedinger, H. C. Scraggs, W. Weintraub, and C. H. Yu, Phys. Rev. C **58**, 801 (1998).
[16] C. M. Petrache, G. Lo Bianco, P. G. Bizzeti, A. M. Bizzeti-Sona, D. Bazzacco, S. Lunardi, M. Nespolo, G. de Angelis, P. Spolaore, N. Blasi, S. Brant, V. Krstić, and D. Vretenar, Eur. Phys. J. A **14**, 439 (2002).
[17] P. A. Wilmarth, J. M. Nitschke, R. B. Firestone, and J. Gilat, Z. Phys. A **325**, 485 (1986).
[18] V. Medina-Chico, M. Sc. thesis, University of Manchester, 2000.
[19] C. N. Davids *et al.*, Nucl. Instrum. Methods Phys. Res. B **40/41**, 1224 (1989); **70**, 358 (1991).
[20] D. C. Radford, Nucl. Instrum. Methods Phys. Res. A **361**, 297 (1995); **361**, 306 (1995).
[21] F. Plasil and M. Blann, Phys. Rev. C **11**, 508 (1975).
[22] T. Morek, K. Starosta, Ch. Droste, D. B. Fossan, G. J. Lane, J. M. Sears, J. F. Smith, and P. Vaska, Eur. Phys. J. A **3**, 99 (1998).
[23] S. Pilotte, S. Flibotte, S. Monaro, N. Nadon, D. Prévost, P. Taras, H. R. Andrews, D. Horn, V. P. Janzen, D. C. Radford, D. Ward, J. K. Johansson, J. C. Waddington, T. E. Drake, A. Galindo-Uribarri, and R. Wyss, Nucl. Phys. **A514**, 545 (1990).
[24] C. J. Chiara, Ph. D. thesis, State University of New York at Stony Brook, 2001; C. J. Chiara, A. J. Boston, J. Cardona, H. J. Chantler, R. J. Charity, M. P. Carpenter, P. T. W. Choy, C. N. Davids, M. Devlin, A. M. Fletcher, D. B. Fossan, S. J. Freeman, R. V. F. Janssens, N. S. Kelsall, T. Koike, D. R. Lafosse, M. J. Leddy, P. J. Nolan, E. S. Paul, D. G. Sarantites, D. Seweryniak, J. F. Smith, K. Starosta, R. Wadsworth, A. N. Wilson, and Z. Ye (unpublished).
[25] R. Bengtsson and S. Frauendorf, Nucl. Phys. **A327**, 139 (1979).
[26] S. M. Harris, Phys. Rev. **138**, B509 (1965).
[27] D. M. Todd, R. Aryaeinejad, D. J. G. Love, A. H. Nelson, P. J. Nolan, P. J. Smith, and P. J. Twin, J. Phys. G **10**, 1407 (1984).
[28] R. Wyss, A. Granderath, R. Bengtsson, P. Von Brentano, A. Dewald, A. Gelberg, A. Gizon, J. Gizon, S. Harissopulos, A. Johnson, W. Lieberz, W. Nararewicz, J. Nyberg, and K. Schiffer, Nucl. Phys. **A505**, 337 (1989).
[29] A. Granderath, P. F. Mantica, R. Bengtsson, R. Wyss, P. von Brentano, A. Gelberg, and F. Seiffert, Nucl. Phys. **A597**, 427 (1996).
[30] R. Wyss, J. Nyberg, A. Johnson, R. Bengtsson, and W. Nazarewicz, Phys. Lett. B **215**, 211 (1989).
[31] W. Nazarewicz, G. A. Leander, and A. Johnson, Nucl. Phys. **A503**, 285 (1989).
[32] D. Ward, H. R. Andrews, V. P. Janzen, D. C. Radford, J. K. Johansson, D. Prévost, J. C. Waddington, A. Galindo-Uribarri, and T. E. Drake, Nucl. Phys. **A529**, 315 (1991).
[33] W. Nazarewicz, J. Dudek, R. Bengtsson, and I. Ragnarsson, Nucl. Phys. **A435**, 397 (1985).
[34] S. Cwiok, J. Dudek, W. Nazarewicz, W. Skalski, and T. Werner, Comput. Phys. Commun. **46**, 379 (1987).
[35] R. Wyss, F. Lidén, J. Nyberg, A. Johnson, D. J. G. Love, A. H. Nelson, D. W. Banes, J. Simpson, A. Kirwan, and R. Bengtsson, Nucl. Phys. **A503**, 244 (1989).
[36] H. J. Chantler, E. S. Paul, A. J. Boston, C. J. Chiara, P. T. W. Choy, A. M. Fletcher, D. B. Fossan, R. V. F. Janssens, N. S. Kelsall, T. Koike, D. R. LaFosse, P. J. Nolan, D. G. Sarantites, D. Seweryniak, J. F. Smith, K. Starosta, R. Wadsworth, and A. N. Wilson, Phys. Rev. C **66**, 014311 (2002).
[37] J. F. Smith, D. B. Fossan, G. J. Lane, J. M. Sears, I. Thorslund, P. Vaska, I. M. Hibbert, R. Wadsworth, I. Y. Lee, and A. O. Macchiavelli, Phys. Lett. B **483**, 7 (2000).
[38] F. Dönau and S. Frauendorf, in *Proceedings of the Conference on High Angular Momentum Properties of Nuclei, Oak Ridge, 1982*, edited by N. R. Johnson (Harwood Academic, New York, 1983), p. 143; F. Dönau, Nucl. Phys. **A471**, 469 (1987).
[39] S. Törmänen, S. Juutinen, R. Julin, B. Cederwall, A. Johnson, R. Wyss, P. Ahonen, B. Fant, M. Matsuzaki, J. Nyberg, M. Piiparinen, S. Mitarai, J. Mukai, and A. Virtanen, Nucl. Phys. **A572**, 417 (1994).
[40] T. Lönnroth, S. Vajda, O. C. Kistner, and M. H. Rafailovich, Z. Phys. A **317**, 215 (1984).
[41] A. Bohr and B. R. Mottelson, *Nuclear Structure*, Nuclear Deformations Vol. II (World Scientific, Singapore, 1998).